JGR Oceans

RESEARCH ARTICLE
10.1029/2019JC015404

Key Points:
- Submesoscales in the northeastern SCS were investigated based on 1/30° OFES model
- The regions southwest of Taiwan and Luzon Strait are two submesoscales hot spots but have different seasonality
- Submesoscales in regions ST and LS are generated by mixed-layer instability and barotropic instability, respectively

Supporting Information:
- Supporting Information S1

Correspondence to:
Z. Zhang,
zzw330@ouc.edu.cn

Citation:
Zhang, Z., Zhang, Y., Qiu, B., Sasaki, H., Sun, Z., Zhang, X., et al (2020). Spatiotemporal characteristics and generation mechanisms of submesoscale currents in the northeastern South China Sea revealed by numerical simulations. *Journal of Geophysical Research: Oceans*, *125*, e2019JC015404. https://doi.org/10.1029/2019JC015404

Received 20 JUN 2019
Accepted 29 JAN 2020
Accepted article online 03 FEB 2020

Spatiotemporal Characteristics and Generation Mechanisms of Submesoscale Currents in the Northeastern South China Sea Revealed by Numerical Simulations

Zhiwei Zhang[1,2], Yuchen Zhang[1], Bo Qiu[3], Hideharu Sasaki[4], Zhongbin Sun[1], Xincheng Zhang[1], Wei Zhao[1,2], and Jiwei Tian[1,2]

[1]Physical Oceanography Laboratory/IAOS and Frontiers Science Center for Deep Ocean Multispheres and Earth System, Ocean University of China, Qingdao, China, [2]Laboratory for Ocean Dynamics and Climate, National Laboratory for Marine Science and Technology, Qingdao, China, [3]Department of Oceanography, University of Hawai'i at Mānoa, Honolulu, HI, USA, [4]Application Laboratory, Japan Agency for Marine-Earth Science and Technology, Yokohama, Japan

Abstract Although both geostrophic-balanced mesoscale eddies and unbalanced small-scale processes have been well studied in the northeastern South China Sea (NE-SCS), less attention has been devoted to the submesoscales in between (i.e., *O*(1–10 km)), which is recognized as an important conduit connecting the balanced and unbalanced motions. Based on the output from a 1/30° OGCM simulation, spatiotemporal characteristics and generation mechanisms of submesoscales in the NE-SCS are investigated in this study. Through examining the submesoscale relative vorticity and vertical velocity, the regions southwest of Taiwan (ST) and Luzon Strait (LS) are identified as two hot spots of submesoscales in the NE-SCS. Seasonally, the submesoscales in region ST are much stronger in winter than summer, while those in LS do not show a significant seasonality. Statistical analysis suggests that the strength of submesoscales in regions ST and LS is highly correlated with the product of mixed-layer depth and mesoscale strain rate (MSR) and with the MSR itself, respectively. By conducting theoretical scaling and energetics analysis, the authors find that the mixed-layer instability whose strength is determined by the combination of mixed-layer depth and MSR and the barotropic instability associated with current-islands interactions are the dominant generation mechanisms of submesoscales in the above two regions, respectively. Further examinations of the submesoscale energy budget indicate that, to keep a balanced state, the generated submesoscales have to be dissipated by a forward energy cascade, highlighting the important role of submesoscales in the energy balance of the NE-SCS circulation.

Plain Language Summary Oceanic submesoscale currents play important roles in energy budgets and material transport in the upper ocean. Marked by horizontal and temporal scales of *O*(1–10 km) and *O*(1–10 days) at midlatitudes, these currents are poorly studied in the South China Sea. In this study, the spatiotemporal characteristics and generation mechanisms of submesoscales are investigated in the northeastern South China Sea using output from a 1/30° ocean model. Based on the simulated relative vorticity and vertical velocity, the regions southwest of Taiwan and Luzon Strait are identified as two hot spots of submesoscales. In the region southwest of Taiwan, the submesoscales are strong in winter but weak in summer; the submesoscales here are generated primarily through mixed-layer baroclinic instability whose strength is determined by the combination of mixed-layer depth and the deformation rates of mesoscale eddies. For the Luzon Strait, the submesoscales do not have significant seasonality, and their generations are through barotropic instability associated with the current-islands interactions.

1. Introduction

Submesoscale currents (also termed submesoscale turbulence, submesoscales for short hereafter) with spatial and time scales of *O*(1–10 km) and *O*(1–10 days) at midlatitudes, respectively, behave as a dynamical conduit for oceanic energy cascading from geostrophic-balanced motions toward microscale turbulence (Capet et al., 2008b; Gula et al., 2016; McWilliams, 2016). In contrast to mesoscale turbulence, submesoscales are

characterized by $O(1)$ Rossby number, and the nonlinear momentum advection becomes equally important with the Coriolis force. Therefore, it can induce strong vertical motions in the upper boundary layer (e.g., Mahadevan & Tandon, 2006; Thomas et al., 2008; Yu et al., 2019), which are vitally important for biogeochemical processes as well as heat budget in the upper oceans (e.g., Mahadevan et al., 2012; Mahadevan, 2016; Su et al., 2018). Given its importance in energy cascade and vertical material/heat transport, the submesoscales, especially their kinematic characteristics and generation/dissipation mechanisms, have been widely studied in the past decade (see a review by McWilliams, 2016). Examples include those studies in the open oceans (e.g., Buckingham et al., 2019; Callies et al., 2015; du Plessis et al. 2017; Sasaki et al., 2014; Erickson & Thompson, 2018; Gula et al., 2014), but even more studies focus on coastal regions and marginal seas, such as the California Current region (e.g., Capet et al., 2008a, 2008b; Molemaker et al., 2015; Renault et al., 2018), the Gulf of Mexico (e.g., Barkan et al., 2017; Luo et al., 2016; Zhong & Bracco, 2013), and the Mediterranean Sea (e.g., Damien et al., 2017; Pascual et al., 2017).

South China Sea (SCS) is the largest marginal sea in the northwestern Pacific that is featured with abundant and active multiscale dynamical processes (see introduction of Zhang et al., 2017). Over the past decades, both mesoscale eddies and small-scale internal waves and mixing have been extensively investigated, and our knowledge about their kinematics and dynamics have been substantially improved (e.g., Alford et al., 2015; Wang et al., 2003; Yang et al., 2016; Zhang et al., 2013, 2016, and the references therein). Compared to the mesoscale and small-scale processes, the submesoscales in between, however, are poorly studied in the SCS due to its measurement difficulty. Only in recent years have some studies begun paying attention to submesoscales in the SCS and their potential roles in the energy budget and vertical material transport. For example, based on surface drifter and satellite data, Zheng et al. (2008) and Yu et al. (2018) have reported submesoscale vortex train generations in the Luzon Strait (LS) and the western boundary region of the SCS, respectively. Through conducting energy budget analysis for an anticyclonic eddy observed during the SCS Mesoscale Eddy Experiment, Zhang et al. (2016) proposed that transferring energy downscales to submesoscales constituted the dominant dissipation mechanism for the anticyclonic eddy. Based on concurrent hydrographic and microstructure observations along a high-resolution (~2 km) transect across this anticyclonic eddy, Zhong et al. (2017) suggested that the submesoscales possibly produced by mesoscale strain can cause vertical transport at least 1 order of magnitude greater than that by mesoscale eddies; the study of Yang et al. (2017) further pointed out that the elevated mixed-layer turbulent dissipation rate in periphery of the anticyclonic eddy was possibly furnished by these strong unbalanced submesoscales. In addition to observations, some basic features of submesoscales have also been discussed by several high-resolution simulation studies (e.g., Dong & Zhong, 2018; Li et al., 2019; Cao et al., 2019). Despite these efforts made on submesoscales in the SCS in recent years, the statistical spatiotemporal characteristics are largely unrevealed, and generation mechanisms remain elusive.

In open oceans, away from coastal boundaries, mixed-layer baroclinic instability and mesoscale strain-induced frontogenesis are thought as two important generation mechanisms for submesoscales (e.g., Callies et al., 2015; Lapeyre et al., 2006; McWilliams, 2016). Correspondingly, submesoscales tend to be much stronger in winter when mixed layer is deep and they are enhanced in eddy-rich regions such as the western boundary currents and subtropical countercurrent regions (e.g., Buckingham et al., 2016; Callies et al., 2015; Qiu et al., 2014; Sasaki et al., 2014; Su et al., 2018; Thompson et al., 2016). Compared to the open oceans, dynamical background in the SCS especially in its northeastern part is more complex. In addition to seasonally modulated mixed layer and strong eddy activities, the northeastern SCS (NE-SCS; including the LS) also has complicated islands topography that may influence the generation and dissipation of oceanic eddies (Yang et al., 2019; Zheng et al., 2008). Interaction between barotropic tides and the complicated topography in the LS generates large-amplitude internal tides and internal solitary waves (Alford et al., 2015; Li & Farmer, 2011), which can induce strong turbulent mixing that modulates basin-scale circulation in the SCS (Yang et al., 2016; Zhao et al., 2014). Beyond that, dynamics of the NE-SCS circulation is also significantly impacted by the monsoon winds and Kuroshio intrusion (Figure 1; Su, 2004; Gan et al., 2006; Xue et al., 2004; Zhang, Zhao, et al., 2015). However, whether and how such a complex dynamical environment will influence the spatial and seasonal variabilities and generation mechanisms of submesoscales in the NE-SCS are still unclear. In this paper, the above issues will be investigated based on the 1/30° OGCM for the Earth Simulator (OFES) model simulations (Sasaki et al., 2014; Sasaki & Klein, 2012).

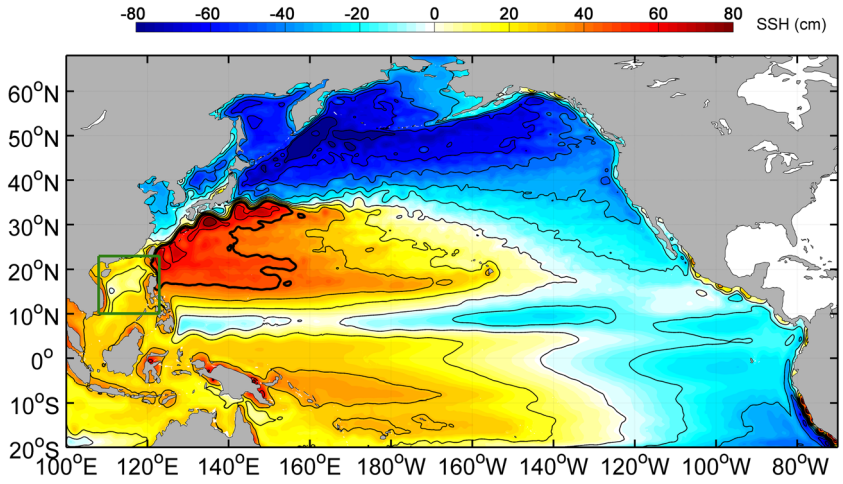

Figure 1. Mean SSH between 2001 and 2003 simulated by the 1/30° OFES model in its whole domain. Black lines are SSH contours with an interval of 15 cm, and the 45-cm SSH contour is highlighted by the thick black line. The green box indicates the SCS that will be analyzed in detail in Figure 2.

The remainder of the paper is organized as follows. Section 2 describes the 1/30° OFES simulation and its comparison with observations in the SCS. Section 3 presents the spatiotemporal characteristics of the submesoscales in the NE-SCS. In section 4, generation mechanisms of submesoscales are analyzed in detail. Finally, the summary and discussion are given in section 5.

2. Model Simulations

2.1. OFES Output Description

In order to investigate the spatiotemporal characteristics and generation mechanisms of submesoscales in the NE-SCS, realistic simulation output from the OFES model at 1/30° (in horizontal) is used in this study. The 1/30° OFES simulation is the extended version of the earlier 1/10° eddy-resolving version (Nonaka et al., 2016; Sasaki et al., 2008), and it has been demonstrated to be capable of partially resolving the submesoscales, especially at middle and low latitudes (Qiu et al., 2014; Sasaki et al., 2014; Sasaki et al., 2017). Atmospheric forcing of the simulation is from the 6-hourly Japanese 25-year reanalysis with 1° resolution (Onogi et al., 2007). Topography of the model is constructed by using the GEBCO One Minute Grid (https://www.gebco.net/) and the JTOPO30 (with half minute resolution near Japan; http://www.mirc.jha.jp/). Vertically, the 1/30° simulation has a total of 100 layers with an enhanced resolution of 5 and ~5–10 m in the upper 100 and 100–200 m layers, respectively. Horizontally, the model domain ranges between 100° E to 70° W in zonal and 20° S to 66° N in meridional, which covers the whole North Pacific and the SCS (Figure 1). Here, the daily mean OFES outputs including temperature, salinity, velocity (both horizontal and vertical), and sea surface height between 1 January 2001 and 31 December 2003 were analyzed in the SCS with particular focus on its northeastern part (see Figure 2).

2.2. Comparison With Observations

Before presenting the detailed analysis, it is necessary to compare the 1/30° OFES output with available observational data to see whether it can adequately simulate the relevant dynamical features in the SCS. Given that the submesoscale activities are strongly influenced by large-scale and mesoscale flows, we first examined the model's performance at the larger scales by comparing the simulated basin-scale circulation and mesoscale eddy kinetic energy (EKE) with the synchronous daily altimeter data obtained from the Copernicus Marine Environment Monitoring Service (http://marine.copernicus.eu/; Figure 2). The used altimeter product has a 1/4° spatial resolution, and it includes sea level anomaly, absolute dynamic topography, and the associated geostrophic velocity. Here, the mesoscale velocity used to calculate EKE is obtained using a 15- to 120-day band-pass filter. Generally, the 1/30° OFES simulation has well reproduced the patterns of both surface circulation and EKE in the SCS. For the mean circulation, the OFES result displays a cyclonic gyre very similar to the altimeter observations, with an intensified western boundary current east

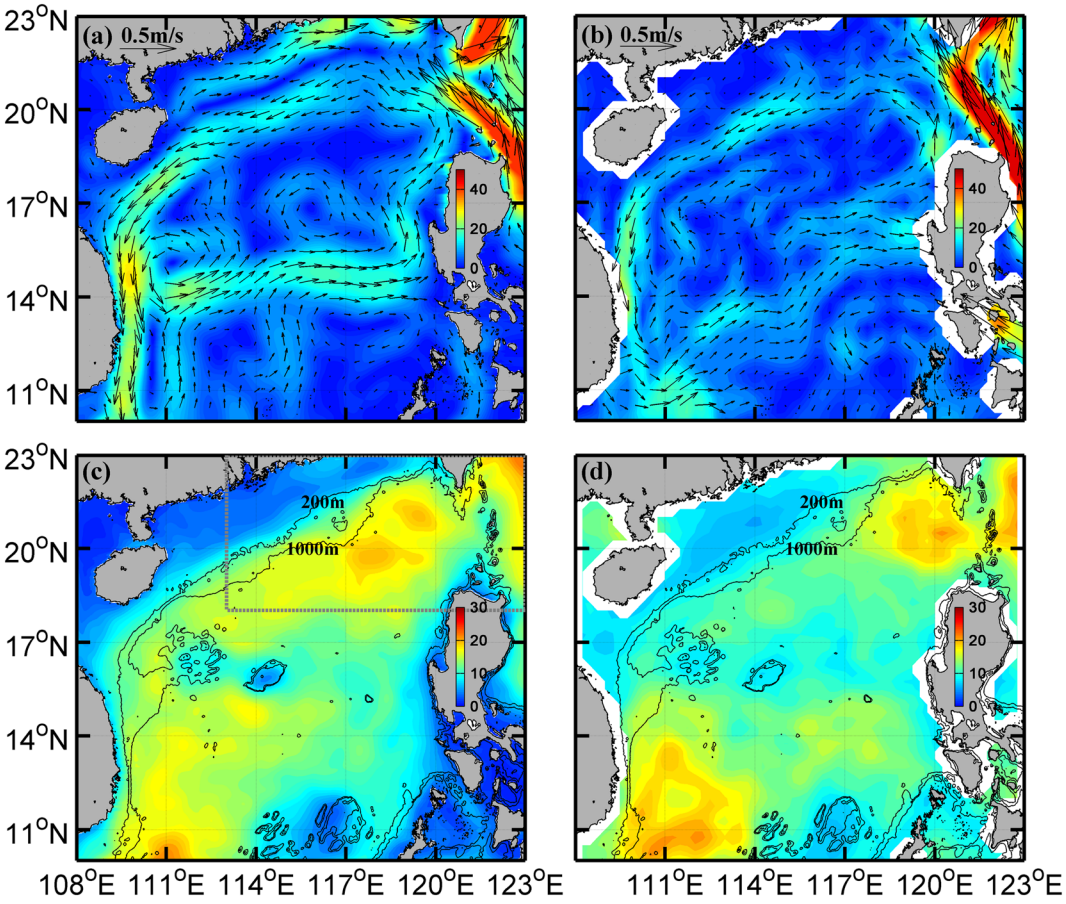

Figure 2. Mean surface circulation in the SCS obtained from (a) the 1/30° OFES simulations and (b) the 1/4° gridded satellite altimeter data between 2001 and 2003. Black vectors and color shadings denote the surface current velocities and their magnitudes (with unit of cm/s), respectively. (c) and (d) are mean magnitudes of the surface mesoscale velocity (i.e., $\sqrt{2 \cdot EKE}$) from the OFES and altimeter data (with unit of cm/s), respectively. Black solid lines indicate the 200- and 1,000-m isobaths. The gray rectangle in (c) indicates the northeastern SCS (113–123°E, 18–23°N), the study region of this paper. Note that because the altimeter data have missed the signals with length scales smaller than 150 km (Qiu et al., 2014, 2016), for a fair comparison, a 150-km low-pass filtering has been applied to the OFES results here.

of Vietnam and a strong Kuroshio current in the LS, as well as a reasonable Kuroshio intrusion southwest of Taiwan (Figure 2a vs. Figure 2b). With respect to the mean EKE, both OFES (Figure 2c) and observations (Figure 2d) show enhanced values in the northeastern and southwestern SCS (more specifically, west of the LS and southeast of Vietnam), respectively. Note that the simulated mean large-scale and mesoscale kinetic energies (KEs) are on average 20–30% higher than the altimeter results. The larger-simulated KE may be caused by the fact that the OFES model is uncoupled to the atmosphere and the damping effect by ocean-atmosphere coupling is therefore not included in this model (e.g., Renault et al., 2017).

In the SCS Mesoscale Eddy Experiment, two submesoscale-resolving (~1-km resolution) shipboard ADCP transects were made across an anticyclonic eddy on 5 December 2013 and 15 January 2014, respectively (Figures 3a and 3b). Here, these two transects of ADCP velocity data are used to examine the 1/30° OFES model's capability in the submesoscale simulation. To this end, wave number spectra of KE in the upper layer (25–80 m) are calculated based on two similar transects across a simulated anticyclonic eddy in the OFES (with close locations and months and similar size and strength to the observation), and they are then compared to the ADCP-derived results (Figures 3c and 3d). The comparison shows that both the OFES and observed KE spectra scale like k^{-2} at the submesoscale range (wavelength less than 80 km), which agrees with that predicted by surface quasi-geostrophic theory modified by ageostrophic advection (Callies & Ferrari, 2013). The similar KE spectral features have also been reported by independent ADCP observations in the northern SCS (Cao et al., 2019). The above result demonstrates that the OFES simulation is able to at least capture the basic features of the submesoscale dynamics.

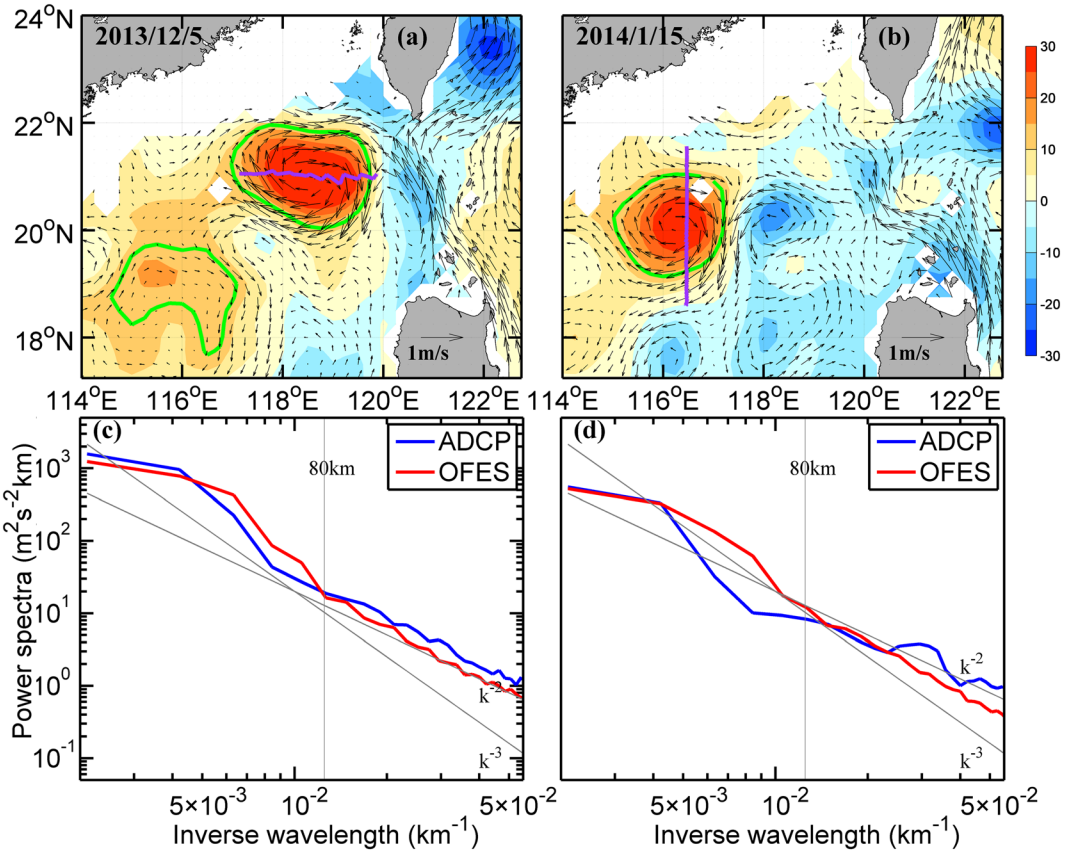

Figure 3. (a, b) Altimeter-observed sea level anomaly (shadings; with unit of cm) and surface absolute geostrophic current (vectors) on 5 December 2013 and 15 January 2014, respectively. The purple line denotes the shipboard ADCP transect across an anticyclonic eddy. The green line roughly indicates edge of the eddy. (c, d) Depth-averaged KE spectrum (between 25 and 80 m) along the transect in (a) and (b). Blue and red lines denote the results calculated using shipboard ADCP and OFES velocity, respectively. For the OFES results, the velocities are chosen along the similar transects in (a) and (b) but across a simulated anticyclonic eddy with similar side, strength, and location to the observations on 13 January and 16 November 2001, respectively. The 80-km wavelength and wave number slops of k^{-2} and k^{-3} are marked by gray lines in (c) and (d).

In order to examine whether the 1/30° OFES model can resolve the mixed-layer instability process, an important generation mechanism of submesoscales, we have estimated the most unstable wavelengths of mixed-layer instability using $L_{MLI} = 2\pi \frac{NH}{f}\sqrt{1 + Ri^{-1}}$, where N, H, f, and Ri are the buoyancy frequency within mixed layer, mixed-layer depth (MLD), Coriolis frequency, and gradient Richardson number ($Ri = N^2 \cdot \left|\partial \vec{U}/\partial z\right|^{-2}$), respectively (Fox-Kemper et al., 2008). The estimated results indicate that in winter, the mean L_{MLI} in the region southwest of Taiwan (region ST) and the LS (referring to the green boxes in Figure 4a) are 23 ± 5 and 25 ± 4 km, respectively. Given that the minimum wavelength the 1/30° OFES model can resolve (i.e., 5 times the model resolution) is ~17 km in the NE-SCS (Sasaki et al., 2017), the above results suggest that the mixed-layer instability that primarily prevails in winter can be well resolved by this model.

3. Spatiotemporal Characteristics

Figures 4a and 4b show the simulated surface relative vorticity ($\zeta = \partial v/\partial x - \partial u/\partial y$) in the NE-SCS on 15 February and 15 August 2003, respectively. On the typical winter day (Figure 4a), the relative vorticity shows strong magnitudes throughout the NE-SCS with the Rossby number ($Ro = \zeta/f$) reaching order one (an important feature of submesoscales). The most prominent submesoscales occur in the regions ST and LS, where elongated submesoscale filaments are abundant with alternatively positive and negative large Rossby

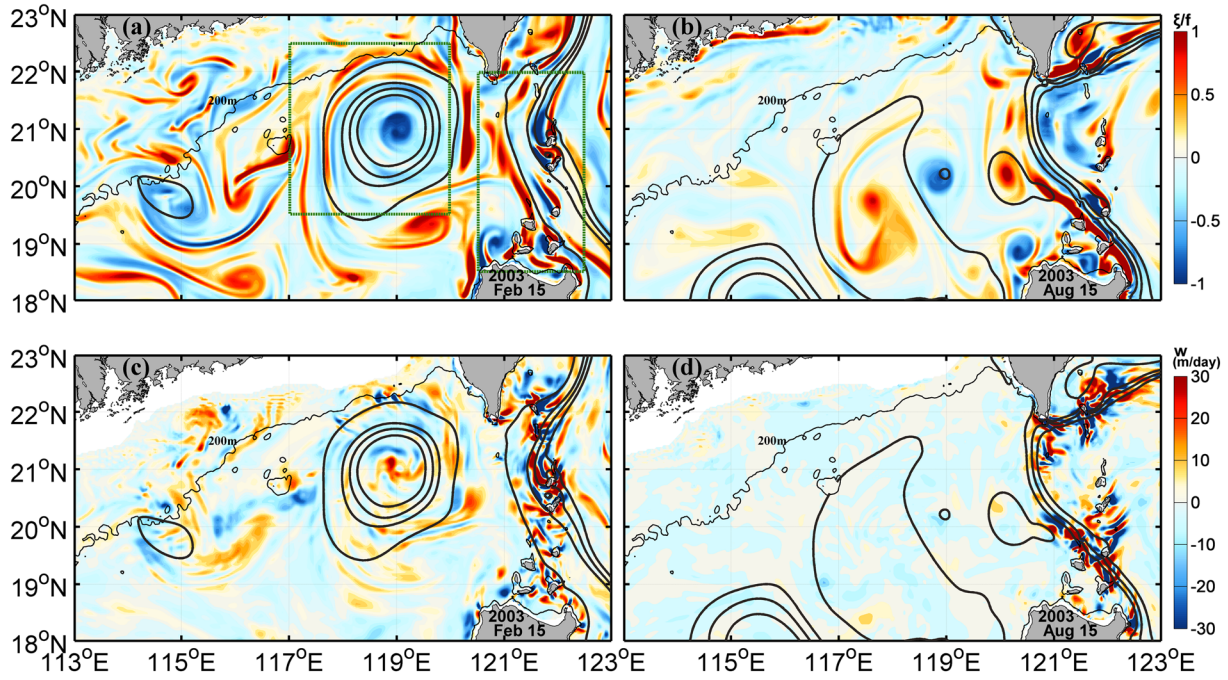

Figure 4. Daily mean distribution of OFES-simulated surface relative vorticity on (a) 15 February and (b) 15 August 2003. The relative vorticity here has been normalized by dividing the planetary vorticity *f*. Black lines are the SSH contours that roughly indicate the Kuroshio axis and the mesoscale eddies. The thin gray line denotes the 200-m isobath. The regions ST and LS that are focused on by this study are marked by green boxes. (c) and (d) are the same as (a) and (b), respectively, but for the vertical velocity (unit m/day) at 50-m depth.

numbers. In the region ST, the submesoscale filaments are primarily located at the periphery of the Kuroshio loop and mesoscale eddies, while for the LS, they prefer to occur in the lee side of the small islands (i.e., Babuyan Islands and Batan Islands) in the Kuroshio path. On the summer day, on the other hand, large Rossby numbers occur only in the LS (Figure 4b). In the SCS interior (including the region ST), the vorticity is dominated by mesoscale eddies with *Ro* generally smaller than 0.3. Corresponding to the large *Ro*, the submesoscale flows have strong divergence and convergence, which produce large vertical velocities (w) at the subsurface layer (Figures 4c and 4d). Note that the w associated with the submesoscales can reach O(10–100 m/day) at 50-m depth, which is 1 to 2 orders larger than that caused by mesoscale eddies.

To obtain statistical insight into the spatial and seasonal variations of submesoscales, in Figures 5a and 5c (Figures 5b and 5d), we show the mean absolute submesoscale *Ro* (w) in winter (in December, January, February, and March) and summer (in June, July, August, and September), respectively. Here, the submesoscale *Ro* and w are obtained based on the 15-day high-pass filtered velocity. The reason why filtering in time rather than space is chosen is to avoid the influence of coast and islands on the filtered results. Actually, if an 80-km high-pass filter is used to isolate the submesoscales, it produces similar magnitudes and spatial patterns for *Ro* and w to the time-filtering results in regions away from coast and islands (see Figure S1 in the supporting information). The seasonal mean $|Ro|$ and $|w|$ of submesoscales generally showed similar spatiotemporal variations as the daily mean results in Figure 4: In the region ST, the submesoscales are strong in winter but weak in summer; in the LS, the submesoscales are strong in both winter and summer, and their magnitudes are comparable. It should be noted that even in winter, the mean strength of submesoscales (for both $|Ro|$ and $|w|$) in LS is on average twice of that in region ST (Figures 5a and 5b). The persistence of strong submesoscales in LS suggests that its generations here may be associated with the islands topography that will be discussed in detail in section 4.

The different seasonality for the submesoscales in regions ST and LS can also be seen from the time series of the region-averaged submesoscale $|Ro|$ and $|w|$(Figure 6). For the region ST, the averaged $|Ro|$ and $|w|$ display a clear annual cycle with the peak and trough occurring in January and June, respectively (Figures 6a and 6c). This seasonality has a good correspondence with the region-averaged MLD, which reaches 50 m in

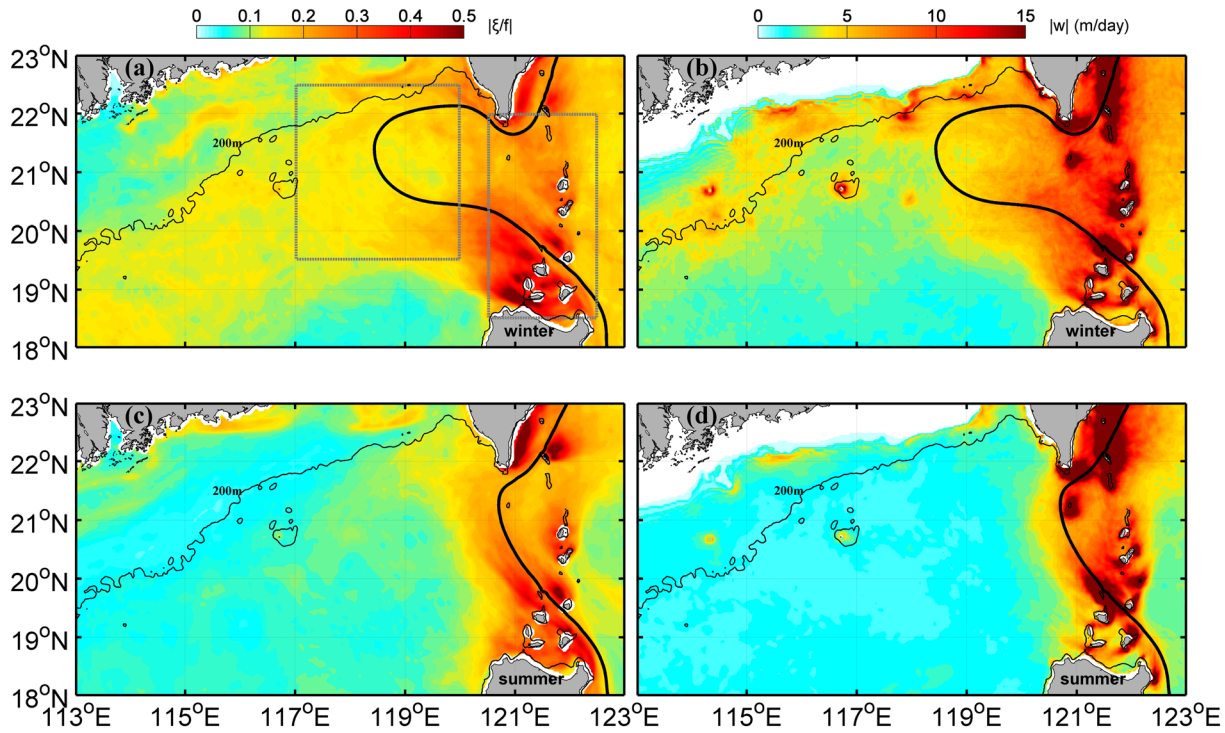

Figure 5. Distribution of (a) mean surface submesoscale |*Ro*| and (b) mean submesoscale |*w*|at 50-m depth in the northeastern SCS in winter. The black line denotes the axis of Kuroshio represented by the SSH contour with the maximum current velocity. (c) and (d) are the same as (a) and (b), respectively, but for summer.

winter but decreases to about 10 m in summer. It is worth pointing out that in winter, the submesoscales are energetic throughout the mixed layer, and large |*Ro*| can still be found beneath the mixed layer base. With respect to the region LS, on the other hand, the seasonal variation of |*Ro*| and |*w*| does not follow the MLD, and they seem to have multiple peaks year round, especially in winter and summer (Figures 6b and 6d). Vertically, |*Ro*| and |*w*| in the regions ST and LS display similar distributions except that the strength of the latter is 1–2 times larger than the former. Additionally, the penetration depth of submesoscales in region LS seems to be larger than that in region ST. For example, in winter, the *e*-folding depth of |*Ro*| is ~200 m in ST, while it can reach ~300 m in LS.

In Figure 7, we show the probability density functions (PDFs) of the submesoscale *Ro* in the two regions. For the near-surface *Ro* in region ST, it shows a strong asymmetry in winter, which has a long tail for large positive values with a skewness of 0.7 (Figure 7a). This phenomenon is similar to previous submesoscale modeling studies and may be ascribed to the combined effect of centrifugal instability and ageostrophic advection that has restricted the large negative vorticities (Klein et al., 2008; Mensa et al., 2013; Zhong & Bracco, 2013). However, in summer and at the 200-m depth (irrespective of winter or summer), such vortical asymmetry becomes insignificant corresponding to the greatly reduced *Ro* (Figures 7a and 7b). In contrast to the ST region, *Ro* in LS displays nearly symmetric distribution in both winter and summer and at both surface and 200 m (Figures 7c and 7d). The probability density for both large positive and negative *Ro* (with |*Ro*|> 1) is 1 to 2 orders larger than that in region ST. Although |*Ro*| generally decreases with depth, the large values are still prevalent at 200-m depth below the mixed layer (Figure 7d). Another notable difference compared with the region ST is that, near the surface, *Ro* in the LS region shows nearly the same PDFs in summer and winter (in agreement with Figures 4 and 5), while at 200-m depth, the probability density of large |*Ro*| is even higher in summer than in winter. It should be noted that although there are more $Ro < -1$ values in region LS compared with region ST, its cumulative proportion is less than 1.3%, suggesting that $Ro = -1$ is indeed a strong lower bound for the anticyclonic vorticities. Furthermore, as will be discussed in detail in section 4.2, the $Ro < -1$ values are mainly confined within small areas in the lee of islands, and they cannot migrate far away from the islands. This phenomenon is similar to the recent simulations of topographic wakes

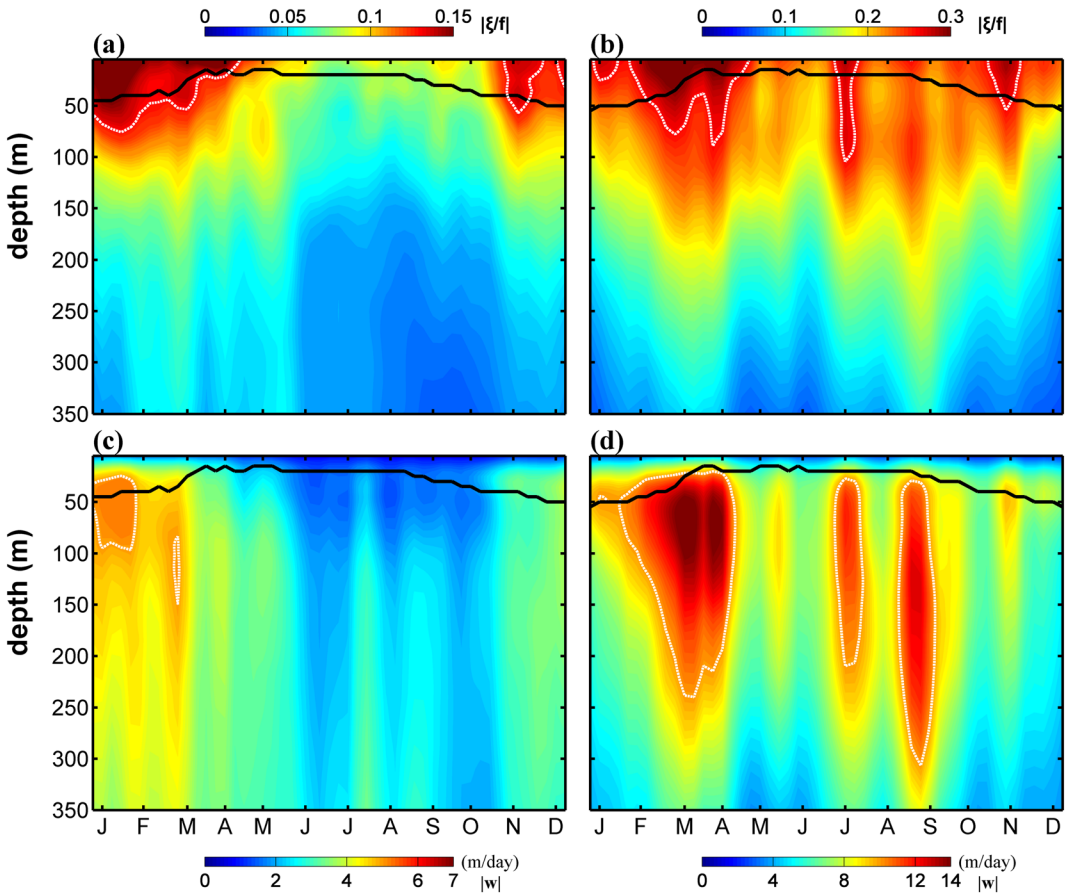

Figure 6. Region-averaged profiles of the climatologically mean submesoscale $|Ro|$ plotted as a function of month in region (a) ST and (b) LS. The black line denotes the region-averaged MLD. The white lines in (a) and (b) denote the $|Ro|$ contours of 0.1 and 0.2, respectively. (c) and (d) are the same as (a) and (b), respectively, but for the submesoscale $|w|$. The white lines in (c) and (d) denote the$|w|$contours of 5 and 10 m/day, respectively.

(Srinivasan et al., 2019), and it helps support the notion that centrifugal instability is an efficient way to dissipate the $Ro < -1$ relative vorticities.

All the above-described contrasting characteristics of submesoscales between regions ST and LS suggest that their generation mechanisms may differ a lot in these two regions. For the former region, the generation of submesoscales may be closely associated with the mixed-layer processes, while for the latter, the mixed-layer processes should not be dominant, and the islands topography may play an important role. In the following section, we will explore in detail the generation mechanisms of submesoscales in the two regions.

4. Generation Mechanisms

4.1. Roles of MLD and Mesoscale Strain

To obtain physical insights into the generations of submesoscales in the NE-SCS, we first examine the geographic distribution of MLD and mesoscale strain rate (MSR) in different seasons (Figure 8), which are widely thought as two important factors modulating the sumesoscale generations (e.g., McWilliams, 2016). For the former, it determines to a large degree the amount of available potential energy that can be released through mixed-layer instability (Callies et al., 2015; Qiu et al., 2014), while for the latter, it is a metric for the strength of horizontal shear and deformation of mesoscale currents that can intensify the pre-existing fronts through frontogenesis (Capet et al., 2008a; Lapeyre et al., 2006). Here, MLD is defined as the depth where potential density exceeds the surface density by 0.03 kg/m^3, and MSR is calculated as $\sqrt{\left(\frac{\partial u_m}{\partial x}-\frac{\partial v_m}{\partial y}\right)^2+\left(\frac{\partial u_m}{\partial y}+\frac{\partial v_m}{\partial x}\right)^2}$, where $\vec{u}_m$ denotes the mesoscale velocity obtained using a 15- to 120-day

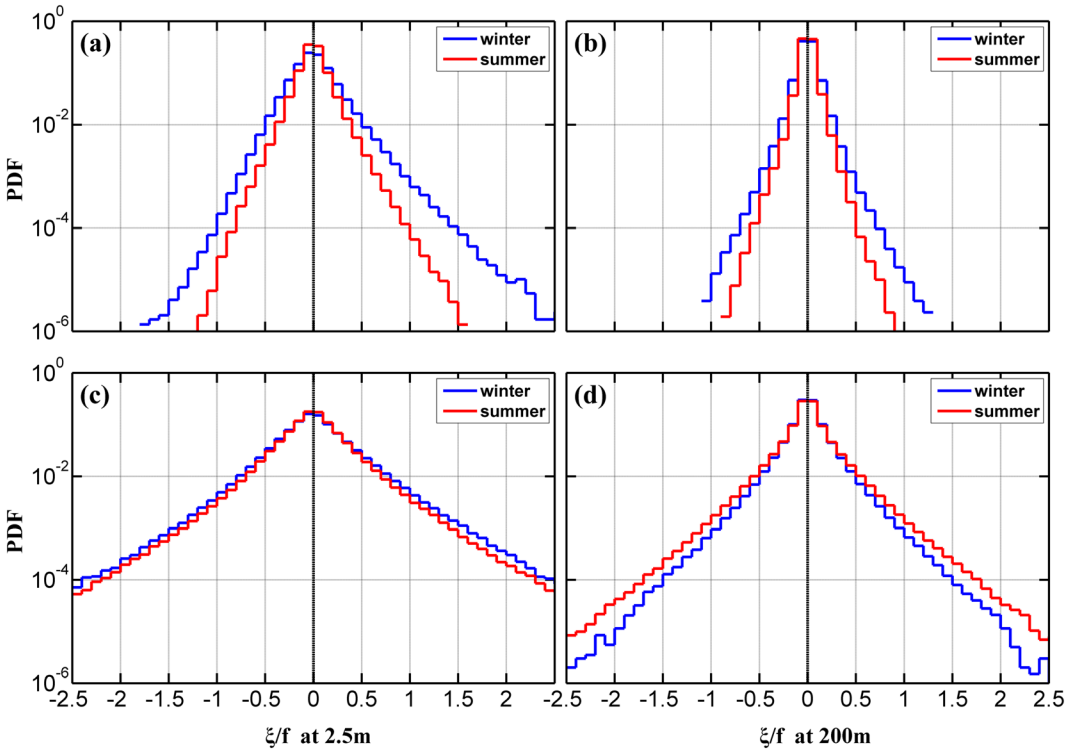

Figure 7. Probability density distribution of the submesoscale *Ro* at (a) 2.5- and (b) 200-m depth in region ST. The blue and red lines denote the results in winter and summer, respectively. (c) and (d) are the same as (a) and (b), respectively, but for the results in region LS.

band-pass filter. It can be clearly seen that the MLD in both the regions (ST and LS) has a noticeable seasonality with the value in winter more than triple that in summer (50–70 m vs. 10–20 m; Figures 8a and 8c). Due to the convergence of near-surface water, the winter-time MLD is deepened within the anticyclonic Kuroshio loop, especially in the region ST. In contrast to MLD, the winter enhancement of upper-ocean MSR can only be found in the region ST, and this seasonality is insignificant in the region LS (Figures 8b and 8d). It should be noted that the strong MSR tends to occur at the periphery of Kuroshio loop (mesoscale eddies) and around the islands in regions ST and LS, respectively. This geographic distribution of MSR is generally in agreement with that of the submesoscale $|Ro|$ and $|w|$ (recall Figures 4 and 5). The above results suggest that the mixed layer and mesoscale strain are of equal importance for the generations of submesoscales in region ST, while the latter may play a more important role in region LS.

In order to further explore the roles of MLD and MSR in the submesoscale variations, we compare the region-averaged time series of MLD and surface MSR with the strength of submesoscales in Figure 9. Because the submesoscales are characterized by both strong relative vorticity and vertical velocity, here, we use the time series of surface $|Ro|$ multiplied by $|w|$ at 50 m as the metric of the strength of submesoscales and define its normalized time series as the submesoscale index (SMI; the normalization is through first removing the time average and then dividing by the standard deviation). However, it should be noted that the conclusion does not change if $|Ro|^2$ or w^2 is used as the SMI. Indeed, in region ST, we can see good correspondence among the three time series with the correlation coefficient (r) between (SMI, MLD) and between (SMI, MSR) reaching 0.44 and 0.70, respectively (Figure 9a). For the time series of SMI and MLD, their correspondence mainly occurs at the annual cycle, as both show high values in winter and low values in summer. It is noticeable that the annual cycle of MLD leads that of SMI, and their r value could reach 0.60 when the former leads the latter by 5 weeks. This time lag is likely due to that the generations of submesoscales cause strong restratification in the mixed layer and therefore shoal the MLD in late winter (du Plessis et al., 2017; Su et al., 2018). The time lag can also be ascribed to the other factors or processes such as MSR and baroclinic frontal arrest that potentially modulate the submesoscale generations (Brannigan

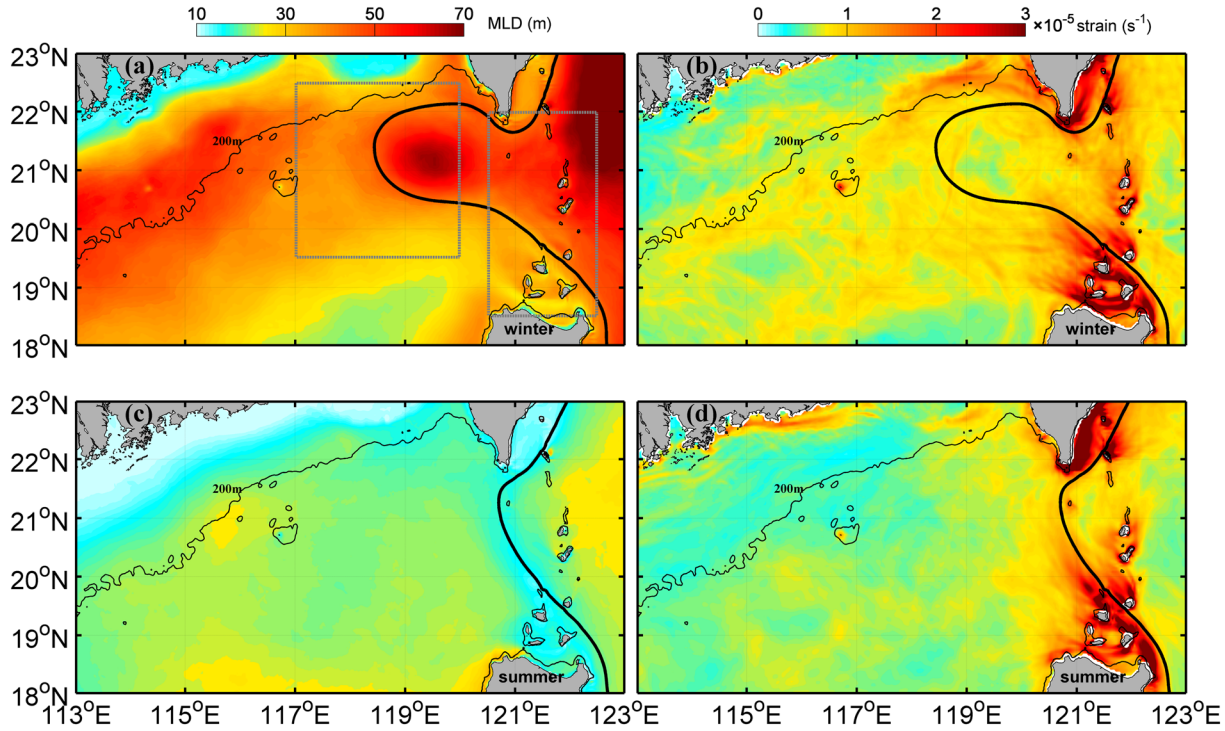

Figure 8. Same as Figure 5 except that shadings in (a) and (c) and (b) and (d) denote MLD and surface MSR, respectively.

et al., 2015; McWilliams & Molemaker, 2011). In addition to the annual cycle, the SMI and MSR also have a good correspondence at the intraseasonal time scale (with periods of 60–90 days), especially in winter. The winter enhancement of intraseasonal MSR is partially associated with the active anticyclonic and cyclonic mesoscale eddy pairs generated by the Kuroshio loop, which is demonstrated to be mainly occur in winter (Zhang et al., 2017). Different from the region ST, the SMI in region LS shows a good correlation only with the MSR ($r = 0.72$), and its correlation with MLD is insignificant ($r = -0.09$; Figure 9b). The correspondence between SMI and MSR mainly occurs at intraseasonal time scale with periods of 60–120 days, and it does not display a clear seasonal modulation. The strong intraseasonal oscillation of MSR can be explained by the westward propagating mesoscale eddies generated in the North Pacific Subtropical Countercurrent region (Qiu, 1999), which interact with the Kuroshio and the islands when they arrive at the LS (Figures 10 and S2; Lien et al., 2014; Zhang, Zhao, et al., 2015). Overall, the correlation analysis in Figure 9 confirms the potential roles played by MLD and MSR (MSR) in the submesoscale generations in region ST (LS) as argued in the previous paragraph.

If the SMI in region ST is compared with the product of MLD and MSR, we find that these two time series become better correlated with the correlation coefficient as high as 0.76 (Figure 11a). This result indicates that the submesoscales in region ST are most likely generated by mixed-layer baroclinic instability (or mixed-layer instability; Callies et al., 2016). For the deep mixed layer in winter, it provides more space to store the available potential energy that can be released to feed baroclinic instability. With respect to the mesoscale strain, it can strengthen the front through frontogenesis and thus increase $|\nabla_h \rho|$ (where ρ is the sea water density). Indeed, good correlations can be found between MSR and mesoscale frontogenesis tendency (F) and between F and $|\nabla_h \rho|$, with their correlation coefficients reaching 0.72 and 0.91, respectively (Figure 11b). Here, F is defined as $F = \mathbf{Q_s} \cdot \nabla_h \rho$ with $\mathbf{Q_s} = -\frac{\partial \rho}{\partial x}\nabla_h u_m - \frac{\partial \rho}{\partial y}\nabla_h v_m$, and it represents the strength of frontognesis by mesoscale horizontal advection (Capet et al., 2008a; Gula et al., 2014). Given that the potential energy per unit depth of a front scales with $|\rho'|^2$ and $|\rho'|^2$ itself scales with $L_f{}^2 \cdot |\nabla_h \rho|^2$ (where L_f is horizontal scale of the front; see Vallis, 2006), it is therefore the combination of MLD and MSR that finally determines the total amount of available potential energy and the strength of mixed-layer instability temporally.

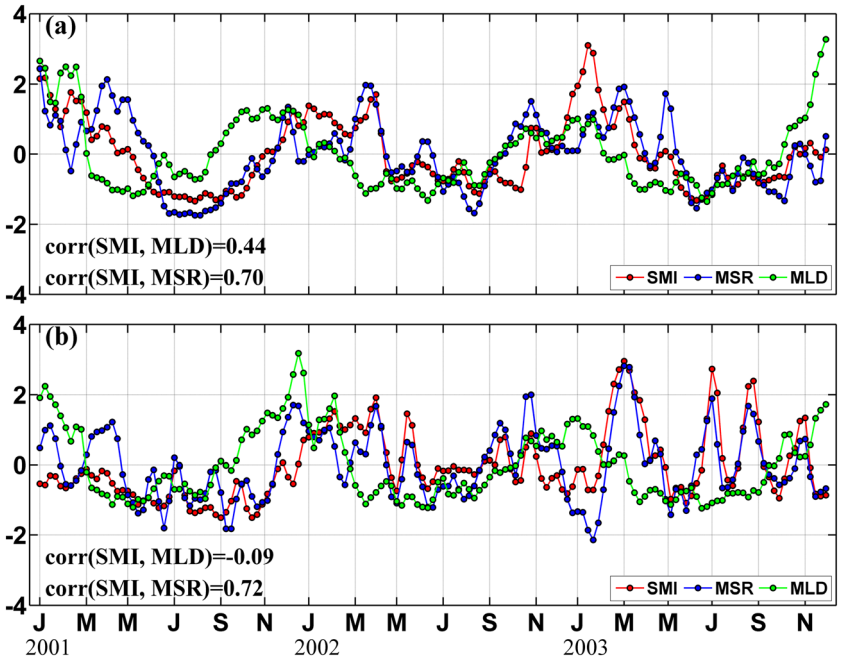

Figure 9. Time series of the weekly SMI (red) and surface MSR (blue) and MLD (green) averaged over (a) region ST and (b) region LS. Correlation coefficients between the different time series are marked in left bottom of the figure. The 95% confidence level of the correlations is 0.19 computed using Monte Carlo method. Note that all the time series have been normalized by subtracting the mean and then being divided by the standard deviation.

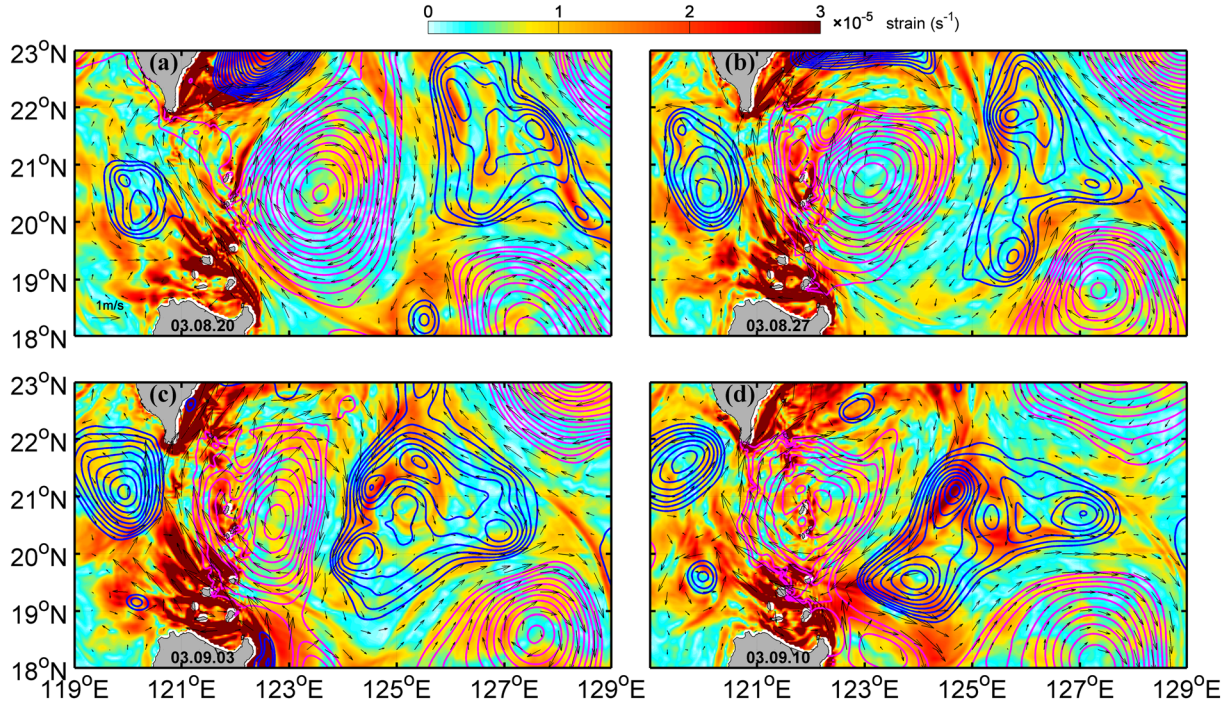

Figure 10. Surface MSR (shading) and sea level anomaly (contours) simulated by the 1/30° OFES model in the Luzon Strait and western Pacific. The pink and blue contours denote the positive and negative sea level anomalies, respectively, with a contour interval of 3 cm. The date is marked on the left bottom corner of each panel.

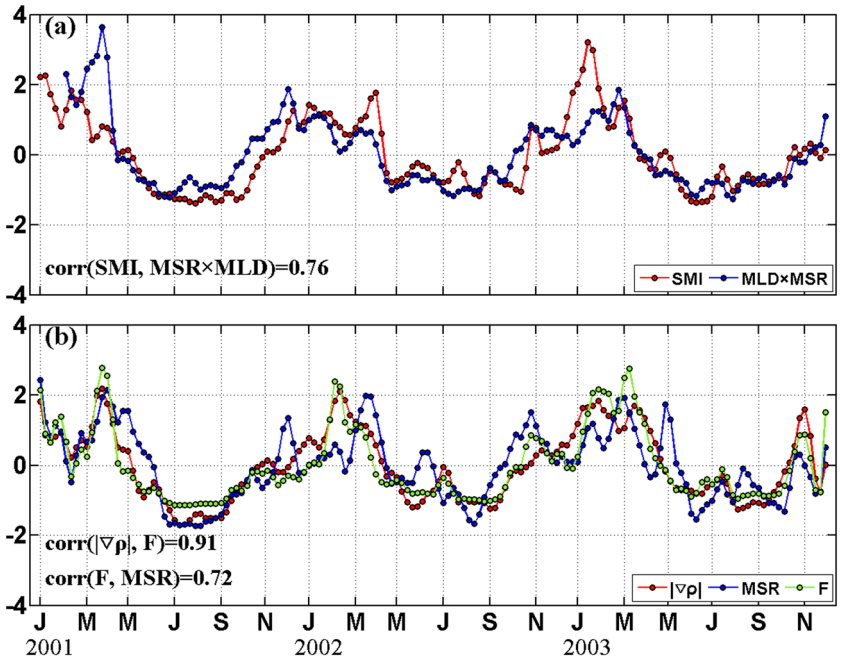

Figure 11. (a) Time series of the weekly SMI (red) and MLD multiplied by surface MSR (green) averaged over region ST. The time series have been normalized by subtracting the mean and then being divided by the standard deviation. Correlation coefficient between the two time series is marked in left bottom of the figure. The 95% confidence level of the correlations is 0.19 computed using Monte Carlo method. (b) Same as (a) except that the red, blue, and green lines denote surface $|\nabla\rho|$ and MSR and frontogenesis tendency (F), respectively.

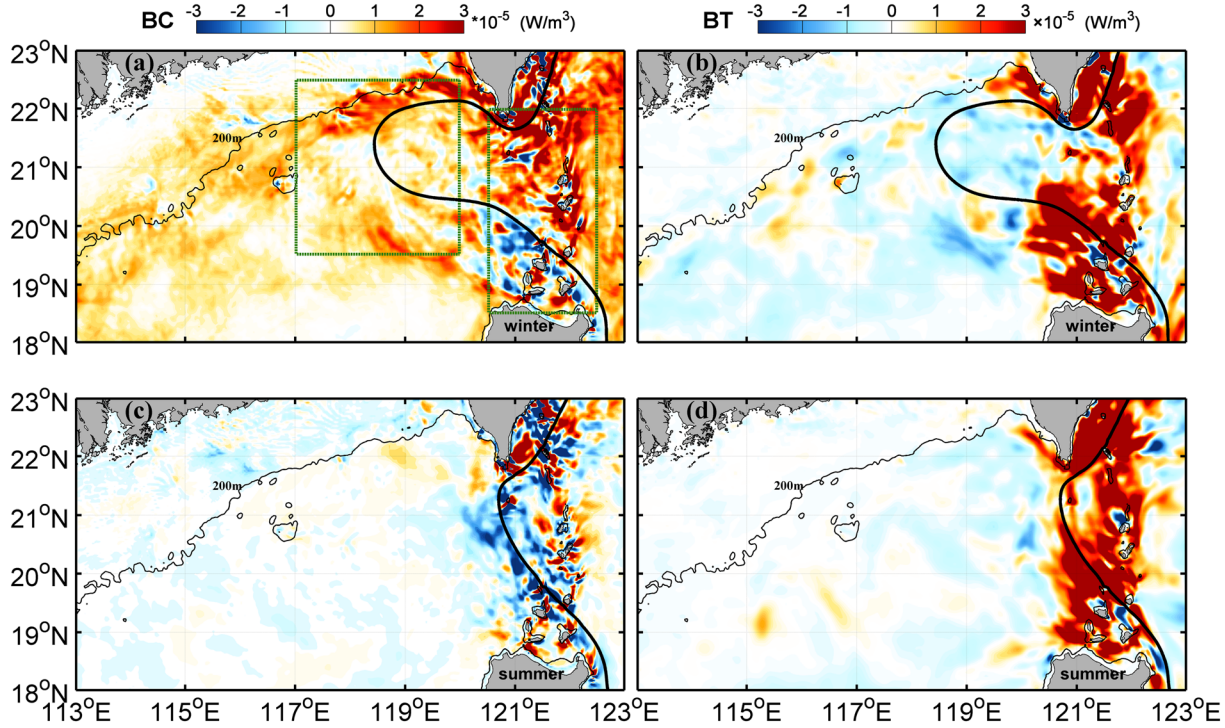

Figure 12. Same as Figure 5 except that shadings in (a) and (c) and (b) and (d) denote depth-averaged BC and BT between 0 and 100 m, respectively.

According to the baroclinic instability theory in Eady's (1949) model (Callies et al., 2015), the wavelength (λ) and growth rate (Δt^{-1}) of the most unstable waves scale with $\frac{NH}{f}$ and $\frac{f\Lambda}{N}$, respectively (where N is stratification in the mixed layer, H is MLD, f is the Coriolis parameter, and Λ is geostrophic velocity shear in vertical). If the thermal wind balance is considered, Δt^{-1} will scale with $\frac{g|\nabla_h\rho|}{\rho_0 N}$. As a result, |u| and |w| of the most unstable wave should scale with $\lambda\cdot\Delta t^{-1} = \frac{gH|\nabla_h\rho|}{\rho_0 f}$ and $H\cdot\Delta t^{-1} = \frac{gH|\nabla_h\rho|}{\rho_0 N}$, respectively. Given that the $|\nabla_h\rho|$ is closely related to MSR (Figure 11b), the above theoretical analysis explains why the strength of submesoscales (i.e., SMI) in region ST is largely determined by the product of MLD and MSR. In the above theoretical framework, we argue that it is the mixed-layer instability that finally energized the submesoscales throughout the mixed layer, and the role of mesoscale strain-driven frontogenesis is to strengthen the fronts and thus increase available potential energy. One supporting argument is that compared to the mixed-layer instability, the submesoscales generated through frontogenesis alone are strongly surface trapped and cannot penetrate below the base of mixed layer as found here (Figure 6; Callies et al., 2016; McWilliams, 2017). However, we are unable to rule out the possibility that some submesoscales, especially those near the surface, are directly induced by frontogenesis. Actually, mixed-layer instability and strain-induced frontogenesis usually co-occur in the real ocean, and they are difficult to be cleanly separated based on the data (McWilliams & Molemaker, 2011; McWilliams, 2016; Srinivasan et al., 2017).

4.2. Energetics Analysis

The results in Figures 9–11 indicate that generations of submesoscales in regions ST and LS are associated with mixed-layer baroclinic instability and mesoscale current-islands interaction, respectively. Here, generation mechanisms of the submesoscales are further examined based on the submesoscale energetics analysis. When external forcing is not taken into account, the baroclinic conversion (BC) and barotropic conversion (BT) terms from mesoscale currents are two primary sources for the submesoscale KE (Capet et al., 2008b). Here, the BC and BT terms are defined as

$$BC = -g\overline{\rho' w'}, \tag{1}$$

$$BT = -\rho_0\left(\overline{u'v'}\frac{\partial\overline{u}}{\partial y} + \overline{u'u'}\frac{\partial\overline{u}}{\partial x} + \overline{u'v'}\frac{\partial\overline{v}}{\partial x} + \overline{v'v'}\frac{\partial\overline{v}}{\partial y}\right), \tag{2}$$

where the prime denotes the submesoscale anomaly (obtained by 15-day high-pass filter) and the overbar denotes the 15-day running mean. From the upper 100-m-averaged energy conversion terms, we can see that in winter, BC is predominantly positive in region ST (Figure 12a), and the large values are in good agreement with the distribution of MSR (Figure 8b). In summer, although BC in region ST still shows positive values, it is 1 order of magnitude smaller than that in winter (Figure 12c). In contrast to region ST, BC in region LS is overall positive (negative) in the northern (southern) part in winter, and it is dominated by large negative values in summer. With regard to the BT term, it does not show a significant seasonality like the BC (i.e., comparable magnitude in winter and summer). Geographically, BT shows strong positive values and weak negative values in regions LS and ST, respectively (Figures 12b and 12d). The large-value BTs mainly occur in the lee side of the islands, which are consistent with the distribution of MSR (Figures 8b and 8d) and the submesoscale |*Ro*| (Figures 5a and 5c) and |*w*| (Figures 5b and 5d). Compared to the BC and BT, the vertical shear production term (*VSP* for short),

$$VSP = -\rho_0\left(\overline{u'w'}\frac{\partial\overline{u}}{\partial z} + \overline{v'w'}\frac{\partial\overline{v}}{\partial z}\right), \tag{3}$$

is 1 order smaller, and therefore, it plays a minor in the submesoscale generations (Figure S3).

The preceding analysis suggests that the BC (BT) term serves as the dominant submesoscale KE source in region ST (LS). In order to demonstrate this point further, we compare the area-averaged BC and BT with SMI in each region (Figure 13). Indeed, SMI in region ST is found to be highly correlated with BC with r reaching 0.74. For the area-averaged BT in region ST, on the other hand, it is negative most of the time, and its correlation with the SMI is negative ($r = -0.31$). In region LS, the situation is reversed. The SMI has a strong correlation with the BT ($r = 0.75$) but a weak correlation with the BC (0.19). Physically, the positive BT and BC in the submesoscale KE budget mean that the submesoscales drain energy from the

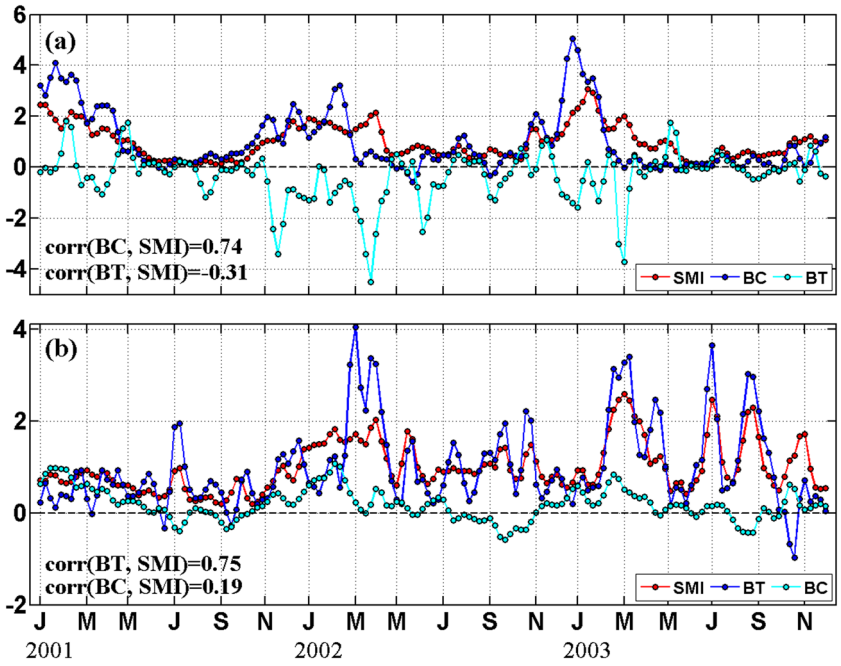

Figure 13. (a) Time series of the weekly SMI (red) and depth-averaged BC (blue) and BT (cyan) averaged over region ST. For a better comparison, the BC and BT were normalized by dividing the mean BC, and the SMI was normalized by dividing the mean value of itself. Correlation coefficients between the different time series are marked in left bottom of the figure. The 95% confidence level of the correlations is 0.19 computed using Monte Carlo method. (b) is the same as (a) except that it shows the results in region LS and that the lines denoting BC and BT have interchanged the colors.

mesoscale KE and the submesoscale available potential energy, respectively. For positive BT, it is primarily associated with barotropic instability of the horizontally sheared flow. With respect to positive BC (corresponding to positive vertical buoyancy flux), its effect is slumping of submesoscale fronts and restratification of the mixed layer, which can be caused by both mixed-layer baroclinic instability and frontogenesis (McWilliams, 2016). However, because the secondary circulation of strain-induced frontogenesis is strongly surface trapped, we believe the mixed-layer instability play a more leading role in producing the positive BC (Callies et al., 2016). Additionally, through examining the wave number spectrum of BC in region ST, we find that in winter, it has an energy peak at around 20–30 km (Figure S4). This energy-containing scale roughly agrees with the most unstable wavelength of mixed-layer baroclinic instability in region ST (i.e., 23 ± 5 km), which lends further evidence for the mixed-layer instability mechanism that energizes submesoscales as argued above. We need to note that even though the SMI in region LS shows relatively weak correlation with BC, it does not mean that the mixed-layer instability plays no role. Actually, the area-averaged BC in region LS is still positive in winter, but its contribution is only half of the BT term (see Table 1).

Table 1
Terms in the Submesoscale KE Budget Analysis in Regions ST and LS in Different Seasons

Region (season)	BC	BT	ADV	PW	DIS	DIS/ (BC + BT) (%)
ST (Win.)	7.86	−2.43	1.04	1.65	8.12	150
ST (Sum.)	0.98	−0.87	0.59	2.96	3.66	3,300
LS (Win.)	10.51	21.87	−4.86	−3.19	24.33	75
LS (Sum.)	−0.99	20.58	−3.75	−8.79	7.05	36

Note. Abbreviations of the terms are the same with equation (3), and their values have a unit of 10^{-6} Wm^{-3}. The rightmost column denotes the ratio between DIS and BC + BT. Note that since the submesoscales in region ST are very weak in summer, the large DIS/(BC + BT) in the second column does not make much sense.

The energetics analysis shown in Figures 12 and 13 demonstrates that mixed-layer instability and barotropic instability are the dominant generation mechanisms of submesoscales in regions ST and LS, respectively. For the mixed-layer instability in region ST, it is enhanced in winter especially in the periphery of mesoscale eddies and the Kuroshio loop due to the combined effect of deep MLD and strong MSR. For the barotropic instability in region LS, it is closely associated with the horizontally sheared flows resulting from the current-islands interactions that have strong MSR by nature. The bottom and lateral boundary drags play a fundamental role in generating the strong shear flows, that is, the current velocity is very weak near the islands and sea bottom but strong away

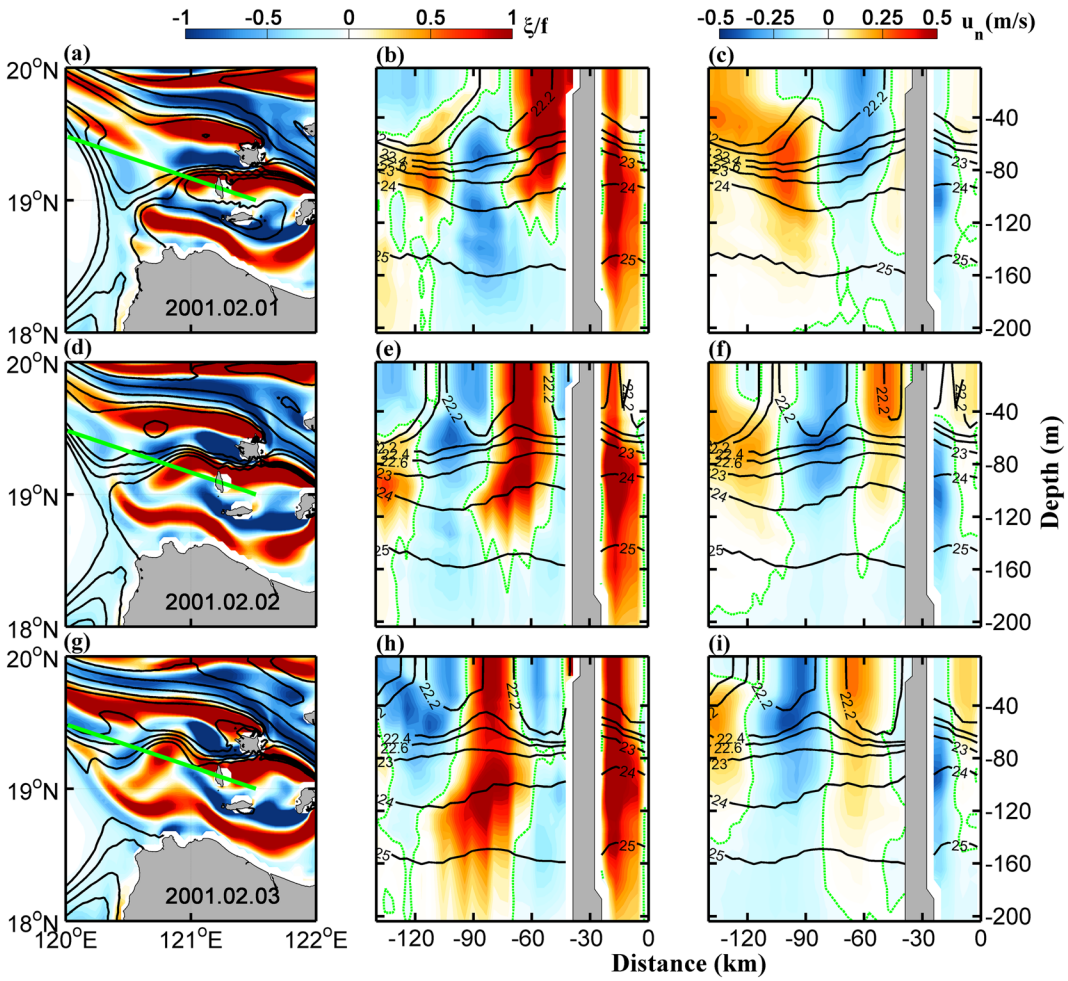

Figure 14. (a) Horizontal distribution of the simulated surface relative vorticity (normalized by *f*) on 1 February 2001. Black lines are the SSH contours that roughly indicate the intensity and direction of currents. (b) Depth-distance distribution of the simulated relative vorticity along the green line in (a) with the distance number starting from eastern end of the line. Black and green lines in (b) denote isopycnals and zero vorticity contour, respectively. (c) Same as (b) but for the normal velocity perpendicular to the section with positive values directing to the right. (d)–(f) and (g)–(i) are the same as (a)–(c), except that they are results on 2 and 3 February 2001, respectively.

from them (Dong et al., 2018; Srinivasan et al., 2019). Due to the strong barotropic instability, the submesoscale eddies quickly grow in the lee of islands, and then they migrate fast downstream by the background current advection (see the example in Figure 14). From vertical structure of the islands wakes in Figure 14 (middle and right columns), one can see that the generated eddies have a diameter of 30–40 km, and they are sometimes subsurface intensified with a core at around 100-m depth. This result suggests that the Kuroshio/eddies-islands interactions in the LS may be an important generation sources for the submesoscale coherent vortices that have been observed in many regions of the world oceans (e.g., McWilliams, 1985; Pelland et al., 2013; Zhang, Li, et al., 2015; Zhang et al., 2019; Li et al., 2017) but are rarely reported in the NE-SCS. Generations of submesoscale coherent vortices in the lee of topography has recently been demonstrated by the high-resolution idealized model simulation (Srinivasan et al., 2019). The submesoscale generations due to mean current-island interaction have also been recently observed in the wake of Palau (e.g., St. Laurent et al., 2019; Merrifield et al., 2019). Previous studies have argued that down-front wind can strengthen the fronts through nonlinear Ekaman transport and therefore may provide favorable conditions for submesoscale generations (Thomas et al., 2008; Thomas & Lee, 2005). However, after comparing the wind velocity along the mesoscale fronts (in down-front direction) with the SMI, we find insignificant correlations between them in nearly the whole study region (figure not shown).

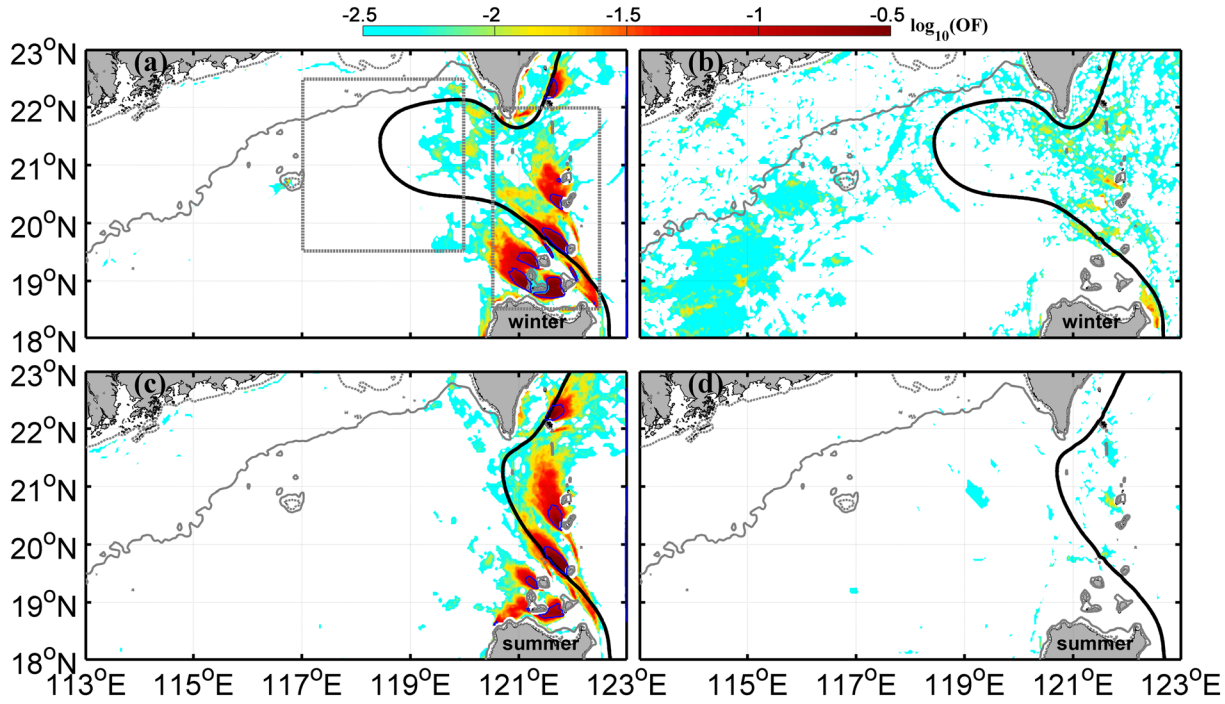

Figure 15. Same as Figure 4 except that shadings in (a) and (c) and (b) and (d) denote the occurrence frequency (OF) of centrifugal instability and symmetric instability at the 22.5-m depth, respectively (i.e., the percentage of time that satisfy the criterion of instability). Note that the color bar is in logarithmic scale (log10). The 0.1 OF contour is indicated by the blue solid line.

This result suggests that the direct wind forcing may play a minor role in the submesoscale generations as compared with the baroclinic and barotopic instabilities in the NE-SCS of our interest.

After quantifying the energy conversion terms in region ST, we find that in winter, although the area-averaged BT is negative that means an inverse KE cascade, the sum of BC and BT is still positive, and its magnitude is more than twice as large as BT itself (5.43×10^{-6} vs. -2.43×10^{-6} Wm^{-3}; see Table 1). In a steady state (neglecting the time derivative term), the submesoscale KE budget is as follows

$$\mathrm{DIS} = \mathrm{BC} + \mathrm{BT} + \mathrm{ADV} + \mathrm{PW}, \tag{4}$$

where $\mathrm{ADV} = -\nabla\cdot\left(\overrightarrow{v}_{\mathrm{m}}\mathrm{KE}\right)$ is the advection of KE ($KE = (u'^2+v'^2)/2$), $\mathrm{PW} = -\nabla_{\mathbf{h}}\cdot\overline{\mathbf{v}'p'}$ is the divergence of perturbative pressure work, and DIS denotes the total of the dissipation terms (Zhang et al., 2016). Due to that ADV and PW are also positive (but with smaller magnitudes than BC + BT), the DIS term in equation (4) has to be positive in order to keep the balance (DIS was 150% of BC + BT; see Table 1). With regard to region LS, although the terms ADV and PW are negative, their magnitudes are much smaller than the KE source term BT + BC (note that BT is much larger than BC). As a result, to keep the KE balance, the DIS term has to account for 75% (36%) of the BC + BT in winter (summer). The above energy budget analysis means that in a steady state, the submesoscale KE in both regions has to be dissipated maybe by smaller-scale processes, which highlights the potential importance of forward KE cascade.

Previous studies have suggested that the centrifugal instability and symmetric instability, which directly transfer the submesoscale KE downward to turbulence, are two important routes for the dissipation of submesoscales (Gula et al., 2016; McWilliams, 2016; Thomas et al., 2013). For the occurrence of centrifugal instability, the criterion is that the absolute vorticity (i.e., $\zeta+f$) is negative in the northern hemisphere; while for the symmetric instability, its occurrence requires negative Ertel potential vorticity (PV) but positive absolute vorticity (Thomas et al., 2013). Here, the Ertel PV is defined as

$$Q_{Ertel} = \vec{\omega}_a \cdot \nabla b = \left(-\frac{\partial v}{\partial z} + \frac{\partial w}{\partial y}\right)\frac{\partial b}{\partial x} + \left(\frac{\partial u}{\partial z} - \frac{\partial w}{\partial x}\right)\frac{\partial b}{\partial y} + (f+\zeta)\frac{\partial b}{\partial z}, \quad (5)$$

where $b = -g\rho/\rho_0$ is the buoyancy. A key signature of symmetric instability is the reduction of PV by the vertical shear. That is, the first and second terms in equation (5), which are often termed the baroclinic components of PV. In contrast, centrifugal instability can occur simply as a result of the barotropic shear. In the work that follows, we quantify the occurrence frequency of both centrifugal and symmetric instabilities, where we assume the latter occurs when the Ri is less than unity but larger than a quarter (Bachman et al., 2017). The occurrence of centrifugal instability is simply the usual criterion, $\zeta + f < 0$. In Figure 15, we calculate and show the occurrence frequency of centrifugal and symmetric instabilities in the NE-SCS upper mixed layer based on their respective criteria described above (only show results at 22.5 m, but it has a similar pattern at other depths). It is found that the centrifugal instability primarily occurs in region LT, and its occurrence frequency can reach ~10% in the lee side of the islands in both winter and summer (Figures 15a and 15c). In contrast, the symmetric instability rarely occurs in the NE-SCS, and only in some small areas in the lee of islands in winter can its occurrence frequency reach ~1% (Figures 15b and 15d). The above results suggest that in region LS, the centrifugal instability may provide an important route for the submesoscale dissipation; while in region ST, neither of centrifugal and symmetric instabilities are found important, and the submesoscale KE is most possibly dissipated through parameterized viscosity in the model. It should be noted that because the effective horizontal resolution of the model is only 17 km, the high lateral buoyancy gradients (lateral velocity shear) associated with symmetric (centrifugal) instability may not be properly represented. So whether the conclusions regarding the occurrence frequency of symmetric and centrigual instabilities can represent the reality should be verified using even higher-resolution observations and numerical simulations in the future.

5. Summary and Discussion

Over the past several decades, the multiscale oceanic dynamical processes, including both the geostrophically balanced large-scale and mesoscale currents and the unbalanced internal waves and turbulent mixing, have been extensively studied in the SCS. However, the submesoscales that connect the balanced and unbalanced motions remain to a large degree unexplored due to the difficulty in observations, which has become the major knowledge gap in studying the energy cascade among the multiscale processes in the SCS. Based on the state-of-the-art 1/30° OFES simulation, we have in this work investigated the spatiotemporal characteristics and generation mechanisms of the submesoscales in the NE-SCS. After obtaining the submesoscale currents using a 15-day high-pass filter (similar for a 80-km space filter), the regions ST and LS are identified as two hot spots of submesoscales that show large Ro and strong vertical velocities with magnitudes of $O(1)$ and O(10–100 m/day), respectively. Further analysis shows that the submesoscales in these two regions have quite different characteristics and generation mechanisms.

Phenomenologically, the submesoscales in region ST primarily occur in winter and along the periphery of mesoscale eddies (and also Kuroshio loop) where MSR is enhanced. The submesoscales in region LS, on the other hand, does not display a significant seasonality and is mainly located in the lee of islands. Another notable difference between the two regions is that the submesoscales in LS are much stronger than that in ST both in terms of the strength ($|Ro|$ and $|w|$) and the penetration depth. Statistically, the submesoscales in region ST have good correlations with both MLD and MSR, while it shows a significant correlation only with MSR in region LS.

Corresponding to the different spatiotemporal characteristics, the generation mechanisms of submesoscales are also different in the two regions. For the submesoscales in region ST, their generation is found to be closely associated with the mixed-layer baroclinic instability. Because that it is the combination of MLD and $|\nabla_h \rho|$ that determines the amount of available potential energy feeding the mixed-layer instability and that $|\nabla_h \rho|$ is strongly modulated by the MSR through buoyancy advection and frontogenesis, it explains why the SMI is highly correlated with the product of MLD and MSR. This result is actually consistent with the existing submesoscale parameterization that the submesoscale vertical buoyancy flux scales with $\mathrm{MLD}^2 \cdot |\nabla_h \rho|^2$ (Fox-Kemper et al., 2008). The conclusion that submesoscales in region ST are generated through mixed-layer instability is also demonstrated by the strong (weak) BC in winter (summer) based on the energetics analysis. It should be noted that the seasonality of submesoscales in region ST (i.e., stronger in winter and

weaker in summer) is essentially not determined by the state of the Kuroshio but by the total available potential energy stored in the mixed layer. Although the Kuroshio loop tends to occur in winter (not always) that can indeed strengthen the MSR in region ST, it is an unstable state and is usually terminated by eddy shedding (Nan et al., 2011; Zhang et al., 2017). A good example to demonstrate the indeterministic role of Kuroshio is that even after the Kuroshio eddy shedding (Kuroshio returns to its usual gap-leaping state), the submesoscales are still very active in region ST in winter (Figure S5).

With respect to region LS, generations of submesoscales are found to be connected to the current-islands interactions that result in strong MSR in the lee of islands. The large MSR here is not only attributed to Kuroshio-islands interaction but also associated with the westward propagating mesoscale eddies from the open Pacific, which impinge on the Kuroshio and islands in the LS. As a result of the Kuroshio/eddies-islands interactions, the MSR, and thus the SMI, does not have a significant seasonality but shows prominent intraseasonal variabilities with periods of 60–120 days (Zhang, Zhao, et al., 2015). Dynamically, growth of submesoscales in region LS is mainly through barotropic instability that extracts KE from the background current (i.e., the BT term). The horizontally sheared flows responsible for the barotropic instability, in essence, are set up by the lateral and bottom boundary drags when the strong currents of Kuroshio and mesoscale eddies encounter the islands (Dong et al., 2007, 2018; Srinivasan et al., 2019). As a result, temporal variation of the associated MSR is strongly modulated by the background KE here ($r = 0.79$). Although the BC in region LS is very small in summer, its mean magnitude in winter is nearly half of the BT, suggesting that the mixed-layer instability or frontogenesis also provides nonnegligible amount of KE for the wintertime submesoscales. Given that the MSR is found to have a good correlation with the $|\nabla_h \rho|$ ($r = 0.45$), it may play an active role in the above processes through strengthening the front. In addition to the Kuroshio/eddies-islands interactions, in realistic LS, the strong internal waves generated by the complicated topography may also influence the generation and evolution of submesoscales. However, because the present OFES is a hydrostatic model without tidal forcing, it has eliminated the occurrence of internal tides and internal solitary waves. Interaction between internal waves and submesoscales in the LS is an interesting topic that need further study with specially designed observations and simulations in the future.

Previous studies in the North Pacific open ocean have suggested that, after generations, the submesoscales tend to transfer their KE inversely to the larger scale (corresponding to a negative BT) under influence of the Earth's rotation (Qiu et al., 2014; Sasaki et al., 2014, 2017). Based on the bulk energetics analysis for the submesoscales, however, we find in this study that the inverse KE cascade is far from enough to explain the fate of submesoscale energy. To keep a balanced state, the submesoscale KE obtained from BC or BT has to be dissipated by smaller-scale processes (i.e., a forward cascade). This dissipation term would account for 150% of the BC + BT in region ST in winter and 75% and 36% in region LS in winter and summer, respectively. By examining the criteria of centrifugal and symmetric instabilities, it is further found that in region LS, the centrifugal instability has a high occurrence frequency both in winter and summer; while in region ST, neither of the instabilities are found active. Therefore, the centrifugal instability may provide an important route for the forward energy transfer from submesoscales to microscale dissipations in region LS, while in region ST, the dissipation of submesoscales may be ascribed to other unresolved processes in the model. By examining the PDF of Ri within the mixed layer, we found that even in winter, the cumulative proportion of $0.25 < Ri < 1$ is only 4% (9%) in region ST (LS) (Figure S6). This low proportion may be caused by the fact that the present 1/30° OFES model can poorly resolve the strong vertical shears associated with symmetric instability (Bachman et al., 2017). In order to quantify the role of symmetric instability in the submesoscale dissipation, even higher-resolution numerical simulations and observations are needed in the future (effective resolution higher than 1 km).

Finally, we acknowledge that the results in this study are primarily qualitative and far from quantitative as the analysis relied on the 1/30° OFES simulation, which only partially resolves the submesoscales (Sasaki et al., 2017). While improving the model resolution in future will certainly depict more details of the submesoscales, we do not think it will substantially change the present conclusions because the upper mixed-layer KE spectrum has a slope of k^{-2} and the submesoscale KE dramatically drops with decreasing horizontal scale (Qiu et al., 2014). For example, based on a higher-resolution simulation (1.5 km in horizontal) in the southwestern tropical Pacific, the study of Srinivasan et al. (2017) also found BC and BT as the primary submesoscale KE sources in the regions far from and near islands, respectively, which is similar to the present conclusion. As a pilot study for a planned submesoscale observational research, the model-based results here

can provide a useful guidance for the design of future observational experiments. It will be important for future observations to improve understanding of submesoscale dynamics in the SCS (i.e., the roles of Kuroshio intrusion and mesoscale eddies in fueling the submesoscales) and to provide in situ data to quantify the capability of OGCMs in better resolving the submesoscales.

Acknowledgments
This work is jointly supported by the National Natural Science Foundation of China (Grants 41706005, 91958205, and 91858203), the National Key R&D Program of China (Grants 2018YFA0605702 and 2016YFC1402605), and the Global Change and Air-sea Interaction Project (Grant GASI-IPOVAI-01-03). The OFES simulation was conducted by using the Earth Simulator under the support of JAMSTEC. The altimeter data used here were downloaded from the Copernicus Marine Environment Monitoring Service (http://marine.copernicus.eu/). The authors thank the editor and two anonymous reviewers for the useful comments that help improve the manuscript. The other data analyzed in this study can be obtained online (https://jumpshare.com/v/tpg6xQEpM8JFnkZEzaiN). The original outputs of the 1/30° OFES simulation are not publicly available at present due to the large volume but can be accessed from the authors upon request.

References

Alford, M. H., Peacock, T., MacKinnon, J. A., Nash, J. D., Buijsman, M. C., Centurioni, L. R., et al. (2015). The formation and fate of internal waves in the South China Sea. *Nature*, *521*(7550), 65–69. https://doi.org/10.1038/nature14399

Bachman, S. D., Fox-Kemper, B., Taylor, J. R., & Thomas, L. (2017). Parameterization of frontal symmetric instabilities. I: Theory for resolved fronts. *Ocean Modelling*, *109*, 72–95.

Barkan, R., McWilliams, J. C., Shchepetkin, A. F., Molemaker, M. J., Renault, L., Bracco, A., & Choi, J. (2017). Submesoscale dynamics in the northern Gulf of Mexico. Part I: Regional and seasonal characterization and the role of river outflow. *Journal of Physical Oceanography*, *47*(9), 2325–2346.

Brannigan, L., Marshall, D. P., Naveira-Garabato, A., & George Nurser, A. J. (2015). The seasonal cycle of submesoscale flows. *Ocean Modelling*, *92*, 69–84.

Buckingham, C. E., Lucas, N. S., Belcher, S. E., Rippeth, T. P., Grant, A. L. M., le Sommer, J., et al. (2019). The contribution of surface and submesoscale processes to turbulence in the open ocean surface boundary layer. *Journal of Advances in Modeling Earth Systems*, *11*(12), 4066–4094. https://doi.org/10.1029/2019MS001801

Buckingham, C. E., Naveira Garabato, A. C., Thompson, A. F., Brannigan, L., Lazar, A., Marshall, D. P., et al. (2016). Seasonality of submesoscale flows in the ocean surface boundary layer. *Geophysical Research Letters*, *43*(5), 2118–2126. https://doi.org/10.1002/2016GL068009

Callies, J., & Ferrari, R. (2013). Interpreting energy and tracer spectra of upper-ocean turbulence in the submesoscale range (1–200 km). *Journal of Physical Oceanography*, *43*, 2456–2474.

Callies, J., Ferrari, R., Klymak, J. M., & Gula, J. (2015). Seasonality in submesoscale turbulence. *Nature Communications*, *6*, 6862.

Callies, J., Flierl, G. R., Ferrari, R., & Fox-Kemper, B. (2016). The role of mixed-layer instabilities in submesoscale turbulence. *Journal of Fluid Mechanics*, *788*, 5–41.

Cao, H., Jing, Z., Fox-Kemper, B., Yan, T., & Qi, Y. (2019). Scale transition from geostrophic motions to internal waves in the northern South China Sea. *Journal of Geophysical Research, Oceans*, *124*(12), 9364–9383. https://doi.org/10.1029/2019JC015575

Capet, X., McWilliams, J. C., Molemaker, M. J., & Shchepetkin, A. F. (2008a). Mesoscale to submesoscale transition in the California Current System. Part II: Frontal processes. *Journal of Physical Oceanography*, *38*, 44–64.

Capet, X., McWilliams, J. C., Molemaker, M. J., & Shchepetkin, A. F. (2008b). Mesoscale to submesoscale transition in the California Current System. Part III: Energy balance and flux. *Journal of Physical Oceanography*, *38*, 2256–2269.

Damien, P., Bosse, A., Testor, P., Marsaleix, P., & Estournel, C. (2017). Modeling postconvective submesoscale coherent vortices in the northwestern Mediterranean Sea. *Journal of Geophysical Research, Oceans*, *122*, 9937–9961. https://doi.org/10.1002/2016JC012114

Dong, C., Cao, Y., & McWilliams, J. C. (2018). Island wakes in shallow water. *Atmosphere-Ocean*, 1–8. https://doi.org/10.1080/07055900.2018.1448750

Dong, C., McWilliams, J. C., & Shchepetkin, A. F. (2007). Island wakes in deep water. *Journal of Physical Oceanography*, *37*, 962–981. https://doi.org/10.1175/JPO3047.1

Dong, J., & Zhong, Y. (2018). The spatiotemporal features of submesoscale processes in the northeastern South China Sea. *Acta Oceanologica Sinica*, *37*(11), 8–18.

Du Plessis, M., Swart, S., Ansorge, I. J., & Mahadevan, A. (2017). Submesoscale processes promote seasonal restratification in the Subantarctic Ocean. *Journal of Geophysical Research, Oceans*, *122*(4), 2960–2975. https://doi.org/10.1002/2016JC012494

Eady, E. T. (1949). Long waves and cyclone waves. *Tellus*, *1*, 33–52.

Erickson, Z. K., & Thompson, A. F. (2018). The seasonality of physically-driven export at submesoscales in the northeast Atlantic Ocean. *Global Biogeochemical Cycles*, *32*, 1144–1162. https://doi.org/10.1029/2018GB005927

Fox-Kemper, B., Ferrari, R., & Hallberg, R. (2008). Parameterization of mixed layer eddies. Part I: Theory and diagnosis. *Journal of Physical Oceanography*, *38*, 1145–1165.

Gan, J., Li, H., Curchitser, E. N., & Haidvogel, D. B. (2006). Modeling South China Sea circulation: Response to seasonal forcing regimes. *Journal of Geophysical Research*, *111*, C06034. https://doi.org/10.1029/2005JC003298

Gula, J., Molemaker, M. J., & McWilliams, J. C. (2014). Submesoscale cold filaments in the gulf stream. *Journal of Physical Oceanography*, *44*, 2617–2643.

Gula, J., Molemaker, M. J., & McWilliams, J. C. (2016). Topographic generation of submesoscale centrifugal instability and energy dissipation. *Nature Communications*, *7*, 12811.

Klein, P., Hua, B. L., Lapeyre, G., Capet, X., Gentil, S. L., & Sasaki, H. (2008). Upper ocean turbulence from high-resolution 3D simulations. *Journal of Physical Oceanography*, *38*, 1748–1763.

Lapeyre, G., Klein, P., & Hua, B. L. (2006). Oceanic restratification forced by surface frontogenesis. *Journal of Physical Oceanography*, *36*(8), 1577–1590.

Li, C., Zhang, Z., Zhao, W., & Tian, J. (2017). A statistical study on the subthermocline submesoscale eddies in the northwestern Pacific Ocean based on Argo data. *Journal of Geophysical Research, Oceans*, *122*, 3586–3598. https://doi.org/10.1002/2016JC012561

Li, J., Dong, J., Yang, Q., & Zhang, X. (2019). Spatial-temporal variability of submesoscale currents in the South China Sea. *Journal of Oceanology and Limnology*, *37*(2), 474–485.

Li, Q., & Farmer, D. M. (2011). The generation and evolution of nonlinear internal waves in the deep basin of the South China Sea. *Journal of Physical Oceanography*, *41*, 1345–1363. https://doi.org/10.1175/2011jpo4587.1

Lien, R. C., Ma, B., Cheng, Y. H., Ho, C. R., Qiu, B., Lee, C. M., & Chang, M. H. (2014). Modulation of Kuroshio transport by mesoscale eddies at the Luzon Strait entrance. *Journal of Geophysical Research, Oceans*, *119*(4), 2129–2142. https://doi.org/10.1002/2013JC009548

Luo, H., Bracco, A., Cardona, Y., & McWilliams, J. C. (2016). Submesoscale circulation in the northern Gulf of Mexico: Surface processes and the impact of the freshwater river input. *Ocean Modelling*, *101*, 68–82.

Mahadevan, A. (2016). The impact of submesoscale physics on primary productivity of plankton. *Annual Review of Science*, *8*, 161–184.

Mahadevan, A., D'Asaro, E., Perry, M., & Lee, C. (2012). Eddy-driven stratification initiates North Atlantic Spring phytoplankton blooms. *Science*, *337*(6090), 54–58. https://doi.org/10.1126/science.1218740

Mahadevan, A., & Tandon, A. (2006). An analysis of mechanisms for submesoscale vertical motion at ocean fronts. *Ocean Modelling*, *14*, 241–256.

McWilliams, J. C. (1985). Submesoscale, coherent vortices in the ocean. *Reviews of Geophysics*, *23*, 165–182.

McWilliams, J. C. (2016). Submesoscale currents in the ocean. *Proceedings of the Royal Society*, *A472*, 20160117.

McWilliams, J. C. (2017). Submesoscale surface fronts and filaments: Secondary circulation, buoyancy flux, and frontogenesis. *Journal of Fluid Mechanics*, *823*, 391–432.

McWilliams, J. C., & Molemaker, M. J. (2011). Baroclinic frontal arrest: A sequel to unstable frontogenesis. *Journal of Physical Oceanography*, *41*(3), 601–619.

Mensa, J. A., Garraffo, Z., Griffa, A., Özgökmen, T. M., Haza, A., & Veneziani, M. (2013). Seasonality of the submesoscale dynamics in the Gulf Stream region. *Ocean Dynamics*, *63*, 923–941.

Merrifield, S. T., Colin, P. L., Cook, T., Garcia-Moreno, C., MacKinnon, J. A., Otero, M., et al. (2019). Island wakes observed from high-frequency current mapping radar. *Oceanography*, *32*(4), 92–101.

Molemaker, M. J., McWilliams, J. C., & Dewar, W. K. (2015). Submesoscale instability and generation of mesoscale anticyclones near a separation of the California Undercurrent. *Journal of Physical Oceanography*, *45*, 613–629. https://doi.org/10.1175/JPO-D-13-0225.1

Nan, F., Xue, H., Chai, F., Shi, L., Shi, M., & Guo, P. (2011). Identification of different types of Kuroshio intrusion into the South China Sea. *Ocean Dynamics*, *61*, 1291–1304. https://doi.org/10.1007/s10236-011-0426-3

Nonaka, M., Sasai, Y., Sasaki, H., Taguchi, B., & Nakamura, H. (2016). How potentially predictable are midlatitude ocean currents? *Scientific Reports*, *6*, 20153.

Onogi, K., Tsutsui, J., Koide, H., Sakamoto, M., Kobayashi, S., Hatsushika, H., et al. (2007). The JRA-25 reanalysis. *Journal of the Meteorological Society of Japan*, *85*(3), 369–432. https://doi.org/10.2151/jmsj.85.369

Pascual, A., Ruiz, S., Olita, A., Troupin, C., Claret, M., Casas, B., et al. (2017). A multiplatform experiment to unravel meso- and submesoscale processes in an intense front (AlborEx). *Frontiers in Marine Science*, *4*, 39.

Pelland, N. A., Eriksen, C. C., & Lee, C. M. (2013). Subthermocline eddies over the Washington continental slope as observed by Seagliders, 2003–09. *Journal of Physical Oceanography*, *43*(10), 2025–2053. https://doi.org/10.1175/JPO-D-12-086.1

Qiu, B. (1999). Seasonal eddy field modulation of the North Pacific Subtropical Countercurrent: TOPEX/Poseidon observations and theory. *Journal of Physical Oceanography*, *29*, 2471–2486.

Qiu, B., Chen, S., Klein, P., Sasaki, H., & Sasai, Y. (2014). Seasonal mesoscale and submesoscale eddy variability along the North Pacific Subtropical Countercurrent. *Journal of Physical Oceanography*, *44*, 3079–3098.

Qiu, B., Chen, S., Klein, P., Ubelmann, C., Fu, L.-L., & Sasaki, H. (2016). Reconstructability of three-dimensional upper-ocean circulation from SWOT sea surface height measurements. *Journal of Physical Oceanography*, *46*, 947–963.

Renault, L., McWilliams, J. C., & Gula, J. (2018). Dampening of submesoscale currents by air-sea stress coupling in the Californian Upwelling System. *Scientific Reports*, *8*(13388), 1–7.

Renault, L., McWilliams, J. C., & Penven, P. (2017). Modulation of the Agulhas Current retroflection and leakage by oceanic current interaction with the atmosphere in coupled simulations. *Journal of Physical Oceanography*, *47*(8), 2077–2100.

Sasaki, H., & Klein, P. (2012). SSH wavenumber spectra in the North Pacific from a high-resolution realistic simulation. *Journal of Physical Oceanography*, *42*, 1233–1241.

Sasaki, H., Klein, P., Qiu, B., & Sasai, Y. (2014). Impact of oceanic-scale interactions on the seasonal modulation of ocean dynamics by the atmosphere. *Nature Communications*, *5*, 5636.

Sasaki, H., Klein, P., Sasai, Y., & Qiu, B. (2017). Regionality and seasonality of submesoscale and mesoscale turbulence in the North Pacific Ocean. *Ocean Dynamics*, *67*, 1195–1216.

Sasaki, H., Nonaka, M., Masumoto, Y., Sasai, Y., Uehara, H., & Sakuma, H. (2008). An eddy-resolving hindcast simulation of the quasi-global ocean from 1950 to 2003 on the Earth Simulator. In W. Ohfuchi, & K. Hamilton (Eds.), *High resolution numerical modelling of the atmosphere and ocean* (pp. 157–185). New York, NY: Springer.

Srinivasan, K., McWilliams, J. C., Molemaker, M. J., & Barkan, R. (2019). Submesoscale vortical wakes in the lee of a seamount. *Journal of Physical Oceanography*, *49*, 1949–1971.

Srinivasan, K., McWilliams, J. C., Renault, L., Hristova, H. G., Molemaker, J., & Kessler, W. S. (2017). Topographic and mixed layer submesoscale currents in the near-surface southwestern tropical Pacific. *Journal of Physical Oceanography*, *47*, 1221–1242.

St. Laurent, L., Ijichi, T., Merrifield, S. T., Shapiro, J., & Simmons, H. L. (2019). Turbulence and vorticity in the wake of Palau. *Oceanography*, *32*(4), 102–109.

Su, J. L. (2004). Overview of the South China Sea circulation and its influence on the coastal physical oceanography near the Pearl River estuary. *Continental Shelf Research*, *24*, 1745–1760.

Su, Z., Wang, J., Klein, P., Thompson, A. F., & Menemenlis, D. (2018). Ocean submesoscales as a key component of the global heat budget. *Nature Communications*, *9*, 775.

Thomas, L. N., & Lee, C. M. (2005). Intensification of ocean fronts by down-front winds. *Journal of Physical Oceanography*, *35*, 1086–1102.

Thomas, L. N., Tandon, A., & Mahadevan, A. (2008). Submesoscale processes and dynamics. In M. Hecht, & H. Hasumi (Eds.), *Ocean modeling in an eddying regime*, *Geophysical. Monograph. Series* (Vol. 177, pp. 17–38). Washington DC: American Geophysical Union.

Thomas, L. N., Taylor, J. R., Ferrari, R., & Joyce, T. M. (2013). Symmetric instability in the Gulf Stream. *Deep Sea Research, Part II*, *91*, 96–110.

Thompson, A. F., Lazar, A., Buckingham, C., Naveira Garabato, A. C., Damerell, G. M., & Heywood, K. J. (2016). Open-ocean submesoscale motions: A full seasonal cycle of mixed layer instabilities from gliders. *Journal of Physical Oceanography*, *46*, 1285–1307.

Vallis, G. K. (2006). *Atmospheric and Oceanic Fluid Dynamics*. Cambridge, UK: Cambridge University Press.

Wang, G., Su, J., & Chu, P. (2003). Mesoscale eddies in the South China Sea observed with altimeter data. *Geophysical Research Letters*, *30*(21), 2121. https://doi.org/10.1029/2003GL018532

Xue, H., Chai, F., Pettigrew, N., Xu, D., Shi, M., & Xu, J. (2004). Kuroshio intrusion and the circulation in the South China Sea. *Journal of Geophysical Research*, *109*, C02017. https://doi.org/10.1029/2002JC001724

Yang, Q., Nikurashin, M., Sasaki, H., Sun, H., & Tian, J. (2019). Dissipation of mesoscale eddies and its contribution to turbulent mixing in the northern South China Sea. *Scientific Reports*, *9*(1), 556. https://doi.org/10.1038/s41598-018-36610-x

Yang, Q., Zhao, W., Liang, X., Dong, J., & Tian, J. (2017). Elevated mixing in the periphery of mesoscale eddies in the South China Sea. *Journal of Physical Oceanography*, *47*, 895–907.

Yang, Q., Zhao, W., Liang, X., & Tian, J. (2016). Three-dimensional distribution of turbulent mixing in the South China Sea. *Journal of Physical Oceanography*, *46*, 769–788.

Yu, J., Zheng, Q., Jing, Z., Qi, Y., Zhang, S., & Xie, L. (2018). Satellite observations of sub-mesoscale vortex trains in the western boundary of the South China Sea. *Journal of Marine Systems*, *183*, 56–62.

Yu, X., Garabato, A. C. N., Martin, A. P., Buckingham, C. E., Brannigan, L., & Su, Z. (2019). An annual cycle of submesoscale vertical flow and restratification in the upper ocean. *Journal of Physical Oceanography*. https://doi.org/10.1175/JPO-D-18-0253.1

Zhang, Z., Li, P., Xu, L., Li, C., Zhao, W., Tian, J., & Qu, T. (2015). Subthermocline eddies observed by rapid-sampling Argo floats in the subtropical northwestern Pacific Ocean in spring 2014. *Geophysical Research Letters*, *42*, 6438–6445. https://doi.org/10.1002/2015GL064601

Zhang, Z., Liu, Z., Richards, K., Shang, G., Zhao, W., Tian, J., et al. (2019). Elevated diapycnal mixing by a subthermocline eddy in the western equatorial Pacific. *Geophysical Research Letters*, *46*(5), 2628–2636. https://doi.org/10.1029/2018GL081512

Zhang, Z., Tian, J., Qiu, B., Zhao, W., Chang, P., Wu, D., & Wan, X. (2016). Observed 3D structure, generation, and dissipation of oceanic mesoscale eddies in the South China Sea. *Scientific Reports*, *6*, 24349. https://doi.org/10.1038/srep24349

Zhang, Z., Zhao, W., Qiu, B., & Tian, J. (2017). Anticyclonic eddy sheddings from Kuroshio loop and the accompanying cyclonic eddy in the northeastern South China Sea. *Journal of Physical Oceanography*, *47*, 1243–1259.

Zhang, Z., Zhao, W., Tian, J., & Liang, X. (2013). A mesoscale eddy pair southwest of Taiwan and its influence on deep circulation. *Journal of Geophysical Research, Oceans*, *118*(12), 6479–6494. https://doi.org/10.1002/2013JC008994

Zhang, Z., Zhao, W., Tian, J., Yang, Q., & Qu, T. (2015). Spatial structure and temporal variability of the zonal flow in the Luzon Strait. *Journal of Geophysical Research, Oceans*, *120*, 759–776.

Zhao, W., Zhou, C., Tian, J., Yang, Q., Wang, B., Xie, L., & Qu, T. (2014). Deep water circulation in the Luzon Strait. *Journal of Geophysical Research, Oceans*, *119*(2), 790–804. https://doi.org/10.1002/2013JC009587

Zheng, Q., Lin, H., Meng, J., Hu, X., Song, Y. T., Zhang, Y., & Li, C. (2008). Sub-mesoscale ocean vortex trains in the Luzon Strait. *Journal of Geophysical Research*, *113*, C04032. https://doi.org/10.1029/2007JC004362

Zhong, Y., & Bracco, A. (2013). Submesoscale impacts on horizontal and vertical transport in the Gulf of Mexico. *Journal of Geophysical Research, Oceans*, *118*, 5651–5668. https://doi.org/10.1002/jgrc.20402

Zhong, Y., Bracco, A., Tian, J., Dong, J., Zhao, W., & Zhang, Z. (2017). Observed and simulated submesoscale vertical pump of an anticyclonic eddy in the South China Sea. *Scientific Reports*, *7*, 44011.